Published in final edited form as:
J Am Chem Soc. 2010 July 21; 132(28): 9753–9763. doi:10.1021/ja102098p.

NMR and DFT Investigation of Heme Ruffling: Functional Implications for Cytochrome *c*

Matthew D. Liptak[†], **Xin Wen**[†,‡], and **Kara L. Bren**[*,†]

[†]Department of Chemistry, University of Rochester, Rochester, New York 14627-0216

Abstract

Out-of-plane (OOP) deformations of the heme cofactor are found in numerous heme-containing proteins and the type of deformation tends to be conserved within functionally-related classes of heme proteins. We demonstrate correlations between the heme ruffling OOP deformation and the ^{13}C and ^{1}H nuclear magnetic resonance (NMR) hyperfine shifts of heme aided by density functional theory (DFT) calculations. The degree of ruffling in the heme cofactor of *Hydrogenobacter thermophilus* cytochrome c_{552} has been modified by a single amino acid mutation in the second coordination sphere of the cofactor. The ^{13}C and ^{1}H resonances of the cofactor have been assigned using one- and two-dimensional NMR spectroscopy aided by selective ^{13}C-enrichment of the heme. DFT has been used to predict the NMR hyperfine shifts and electron paramagnetic resonance (EPR) **g**-tensor at several points along the ruffling deformation coordinate. The DFT-predicted NMR and EPR parameters agree with the experimental observations, confirming that an accurate theoretical model of the electronic structure and its response to ruffling has been established. As the degree of ruffling increases, the heme methyl ^{1}H resonances move upfield while the heme methyl and meso ^{13}C resonances move downfield. These changes are a consequence of altered overlap of the Fe 3*d* and porphyrin π orbitals, which destabilizes all three occupied Fe 3*d*-based molecular orbitals and decreases the positive and negative spin density on the β-pyrrole and meso carbons, respectively. Consequently, the heme ruffling deformation decreases the electronic coupling of the cofactor with external redox partners and lowers the reduction potential of heme.

1. Introduction

The heme cofactor is found in proteins with a diverse range of biological functions and out-of-plane (OOP) distortions of this cofactor are found in many of these proteins.1 These OOP distortions are generally described in terms of normal coordinates of the porphyrin macrocycle,2 with the three most prevalent deformations found in biological systems being ruffling, saddling, and doming (Figure 1). Notably, the type of OOP deformation is typically conserved within functionally-related classes of heme proteins.3 Ruffling is the principal OOP deformation in cytochrome *c* (cyt *c*) electron transfer proteins,4–6 the enzyme-substrate complexes of heme oxygenases7 as well as the IsdG and IsdI heme-degrading enzymes,8 and the NO-carriers such as the nitrophorins and the heme nitric oxide/oxygen binding family of proteins.9–12 Saddling is prominent in peroxidases,13 while doming is

bren@chem.rochester.edu.
[‡]Current address: Department of Chemistry and Biochemistry, California State University, Los Angeles, Los Angeles, CA 90032

Supporting Information Available. Mutagenic primer sequences, *Ht* cyt c_{552} gene sequences, minimal medium recipe, NMRPipe processing scripts, additional NMR spectra, ^{13}C and ^{1}H resonance assignments, EPR simulation parameters, graphical representations of the dihedral angle constraints used in the DFT models, DFT-computed QRO, lowest-unoccupied spin-down MO, and spin density plots, QRO energies, total electronic energies, Löwdin spin densities, DFT-computed heme methyl ^{13}C HFSs for horse cyt *c* and Cartesian coordinates for all stationary points described in this work are available online at http://pubs.acs.org.

typically observed in oxygen storage or transport proteins like myoglobin.14 These conserved OOP distortions have been accorded functional relevance; ruffling is proposed to play a role in determining reduction potential,5,15 while both saddling and doming have been implicated in spin state changes.13,16 To date, the majority of studies of heme conformation have utilized either X-ray crystallography or vibrational spectroscopy. To complement these approaches, it is critical to further develop spectroscopic techniques capable of quantifying heme OOP distortions in solution at atomic resolution, such as nuclear magnetic resonance (NMR) spectroscopy.5,10

The further development of NMR spectroscopy as a probe of heme OOP deformations and an understanding of the relationship between these deformations and the function of the cofactor requires an excellent model system. The cyt *c* family of electron transfer proteins is an ideal system in which to study ruffling. One reason is that many cyts *c* contain highly ruffled heme cofactors with little contribution from other types of distortion (Figure 1),1,5 which will facilitate analyses of experimental data. Secondly, the amount of ruffling among cyt *c* species is variable,4,17 suggesting that mutations near the heme may be utilized to modulate the magnitude of heme ruffling. The covalent attachment of the heme cofactor to the polypeptide via two thioether bonds with a conserved Cys-X-X-Cys-His (CXXCH) motif in cyts *c* is proposed to play a key role in inducing ruffling (Figure 2);4,18,19 this proposal suggests a strategy to manipulate heme ruffling by introducing mutations within or adjacent to this attachment motif. For instance, inspection of the X-ray crystal structures of wild-type (WT) and F7A *Pseudomonas aeruginosa* (*Pa*) cyt c_{551} demonstrates that a point mutation at residue 7, which has a backbone hydrogen-bonding interaction with Cys12 (the first residue in the CXXCH motif), can trigger a change in the magnitude of the ruffling deformation.20,21 An additional consideration when using cyts *c* as model systems for heme ruffling is the axial ligand bonding environment. For cyts *c* with His/Met axial ligation, three distinct axial Met configurations are commonly found in nature: *R*, usually observed in mitochondrial cyts *c*, *S*, often found in bacterial cyts c_8, and fluxional, where the axial Met rapidly interconverts between the *R* and *S* configurations (Figure 2).22–24 A change in Met configuration results in a change in axial Met orientation relative to the heme, which inverts the relative energies of the Fe $3d_{xz}$ and $3d_{yz}$ ($3d_{\pi}$) orbitals.23 The relative energies of these orbitals in turn are a major determinant of the distribution of unpaired electron spin density on the heme as well as the magnetic anisotropy, and thus on the observed chemical shifts (see below). The axial ligand orientation thus must be considered explicitly to assure that conclusions reached about effects of porphyrin OOP distortion on electronic structure are not dependent on a particular axial ligand orientation. *Hydrogenobacter thermophilus* (*Ht*) cyt c_{552} can stabilize any of these three axial Met configurations based upon the identity of residue 64, thus *Ht* cyt c_{552} is an ideal member of the cyt *c* family to use when further developing NMR chemical shifts as probes of the heme ruffling deformation.25–27 WT *Ht* cyt c_{552} has a fluxional axial Met, while the *S* and *R* configurations can be stabilized by the Q64N28 and Q64V29 mutations, respectively. An axial Met configuration change may also be correlated to other conformational changes of the axial Met-bearing loop.30 Based upon sequence and structural alignment of *Ht* cyt c_{552} with *Pa* cyt c_{551}, and by analogy to the enhanced ruffling in F7A *Pa* cyt c_{551}, the A7F mutation is expected to reduce the magnitude of heme ruffling as compared to WT *Ht* cyt c_{552}. Consequently, heme ruffling can be monitored in *Ht* cyt c_{552} for the three most common axial Met configurations by studying six variants: WT, A7F, Q64N, A7F/Q64N, Q64V, and A7F/Q64V.

Nuclear magnetic resonance (NMR) spectroscopy of the oxidized, Fe(III), state of *Ht* cyt c_{552} is expected to be a sensitive probe of the heme ruffling deformation in solution. The low-spin d^5 ($S = ½$) electron configuration of the Fe(III) center results in a hyperfine shift (HFS) contribution to the observed chemical shifts of heme nuclei. The HFS is a sum of the

diamagnetic shift (the shift observed in an isostructural diamagnetic system), the Fermi contact (FC) contribution (resulting from through-bond interactions), and the dipolar or pseudocontact shift (resulting from through-space interactions).31 In low-spin ferric heme, the delocalization of the unpaired electron spin density arising from the Fe(III) center onto the porphyrin macrocycle induces a FC shift at each nucleus of the macrocycle with a magnitude proportional to the fraction of the unpaired spin density localized at that nucleus.31 In low-spin ferric hemes, the heme methyl ^{1}H and ^{13}C shifts are dominated by the FC contribution32 and display a distribution on the heme macrocycle primarily determined by the heme axial ligands and their orientations.23 Regarding effects of heme conformation on FC shifts, previous ^{1}H and ^{13}C NMR studies of synthetic model complexes similar to Fe(III) heme have determined that the spin density is preferentially delocalized onto the β-pyrrole carbons in planar hemes, whereas the spin density is delocalized onto the meso carbons in highly ruffled hemes.33,34 This reorganization of the spin density in highly ruffled model complexes is believed to be a consequence of a ground state electron configuration change from $(d_{xy})^2(d_{xz,yz})^3$ to $(d_{xz,yz})^4(d_{xy})^1$ caused by preferential stabilization of the Fe 3d_{xz}- and 3d_{yz}-based molecular orbitals (MOs) by strong π-acceptor axial ligands based upon ligand field theory (LFT) arguments. However, in biological systems when there has been a comparison of more planar and more ruffled six-coordinate hemes, the NMR results have not been consistent with a ground state electron configuration change.5,10,11,35,36 Instead, these studies have observed a decrease of the average heme methyl ^{1}H shift for increased heme ruffling. (The average chemical shift is used in these studies to minimize the contributions of ligand orientation and heme environment to the shifts, and emphasize effects of heme deformation.) This trend has been rationalized using LFT by a ruffling-induced destabilization of the formally doubly-occupied Fe 3d_{xy}-based MO.5,37 While NMR spectroscopy has proven an excellent probe of the spatial distribution of the unpaired electron spin density in heme complexes, electron paramagnetic resonance (EPR) spectroscopy is a better probe of the *d* orbital energies in transition metal complexes38 Indeed, it has been suggested that increased heme ruffling correlates to increased rhombicity of the electronic **g**-tensor for cyts *c*, which would be consistent with a preferential destabilization of the Fe d_{xy}-based MO.5

A full realization of the potential of NMR and EPR spectroscopy to probe heme ruffling requires a more complete understanding of the electronic structure of six-coordinate hemes than is accessible via LFT. In particular, the NMR HFS and EPR *g*-values of oxidized cyt *c* depend upon the spatial distributions and relative energies of the Fe 3*d*-based MOs, respectively.31,37,38 For metalloporphyrins, density functional theory (DFT) appears to provide a reasonable description of these MOs since a good correlation has been observed between DFT spin densities and NMR HFS.39 Unfortunately, the standard deviation of this correlation (106 ppm) is significantly larger than the chemical shift changes that have been observed in the comparisons of planar and ruffled hemes.5,10,11,35,36 Consequently, it will be necessary to use a more complete theoretical expression to model the NMR HFS changes associated with heme ruffling. While the pioneering efforts to calculate the NMR HFS using DFT and an explicit theoretical expression considered only the Fermi contact term,40 a more general expression for the NMR HFS, in the absence of zero field splitting (ZFS), has been formulated by Moon and Patchkovskii (neglecting the diamagnetic $\boldsymbol{\sigma}_{orb}$ term):41

$$\boldsymbol{\sigma}_{HFS} = \frac{-S(S+1)\mu_B}{3\hbar k T \gamma_I} \mathbf{g} \bullet \mathbf{A}^T \quad (1)$$

where *S* is the electron spin quantum number, μ_B is the Bohr magneton, $\hbar$ and *k* are the Planck and Boltzmann constants, γ_I is the magnetogyric ratio for nucleus *I*, and $\mathbf{A}^T$ is the matrix transpose of the hyperfine coupling tensor. Note that the complete HFS is calculated

by this expression, including the contributions typically called FC and pseudocontact in the NMR literature. This formalism has been extended to account for ZFS by Kaupp and co-workers,42 but low-spin Fe(III) is $S = ½$ and ZFS is only observed when $S > ½$. Fortunately, it is relatively straightforward to calculate both the **g**- and **A**-tensors from a DFT-computed electronic structure description using coupled-perturbed self consistent field (CP-SCF) theory.43 Following a CP-SCF calculation, all of the remaining steps required to predict an NMR HFS from a DFT-computed electronic structure are either scalar or matrix multiplication.

In this study, we utilize site-directed mutagenesis, NMR and EPR spectroscopy, and DFT computations to study the heme ruffling OOP deformation in solution using oxidized *Ht* cyt c_{552} as a model system. The magnitude of the heme ruffling deformation has been manipulated using the A7F point mutation, while we have controlled the configuration of the axial Met residue by varying the identity of residue 64 in order to generalize this study for His/Met-ligated hemes with different Met configurations. NMR spectroscopy has been used to monitor the spin density distribution on the oxidized, Fe(III), heme in variants proposed to have different amounts of ruffling. In addition, we have utilized EPR spectroscopy to probe the influence of heme ruffling on the relative energies of the Fe 3*d*-based MOs. These spectroscopic data have been analyzed within the framework of DFT, which has allowed us to correlate the heme ruffling OOP deformation with several NMR spectroscopic observables and confirm that the heme cofactor is less ruffled in A7F *Ht* cyt c_{552} as compared to WT *Ht* cyt c_{552}, as proposed. Finally, our accurate prediction of the NMR spectroscopic data using DFT has allowed us to interpret the underlying DFT-computed electronic structure in terms of function, namely the relationship between the magnitude of heme ruffling and the electron transfer properties of cyt *c*.

2. Materials and Methods

2.1. Protein Expression and Purification

The pSHC552 (Amp^r) and pSHC552N64 (Amp^r) plasmids containing the WT *Ht* cyt c_{552} and Q64N *Ht* cyt c_{552} genes, respectively, along with the N-terminal signal sequence from *Thiobacillus versutus* cyt c_{550} have been previously described.26,28,44 The pSHC552V64 (Amp^r) plasmid containing the gene encoding Q64V *Ht* cyt c_{552} was prepared from the pSHC552 plasmid using the polymerase chain reaction overlap extension method45 as described previously for the preparation of pSHC552N64.28 Next, the A7F mutation was introduced into the *Ht* cyt c_{552} structural gene within the pSHC552, pSHC552N64, and pSHC552V64 plasmids, using the QuikChange II site-directed mutagenesis kit (Stratagene). The A7F mutagenic primers were designed according the guidelines of the QuikChange II kit and obtained from Integrated DNA Technologies. DNA sequencing at the Functional Genomics Center of the University of Rochester confirmed the sequence of the *Ht* cyt c_{552} gene and the desired mutations for all plasmid constructs used for protein expression. For protein expression and purification, each plasmid was co-transformed with the pEC86 (Cm^r) plasmid, containing the *ccmABCDEFGH* cyt *c* maturation genes,46 into the BL21*(DE3) strain of *E. coli* (Invitrogen). Mutagenic primer and *Ht* cyt c_{552} gene sequences are available in the Supporting Information.

The expression and purification of natural isotopic abundance *Ht* cyt c_{552} was carried out as previously described for WT *Ht* cyt c_{552}.26 In addition, WT *Ht* cyt c_{552} and the mutants A7F, Q64N, Q64V, A7F/Q64N, and A7F/Q64V were expressed in *E. coli* by growth on minimal medium supplemented with [5-^{13}C]-™-aminolevulinic acid (5-^{13}C-ALA, Sigma) yielding 5-^{13}C-ALA *Ht* cyt c_{552} and variants, in which four meso and four α-pyrrole positions of the heme cofactor are selectively ^{13}C-enriched (Figure 2).47 The minimal medium composition is available in the Supporting Information.

2.2. NMR Spectroscopy

All NMR experiments were carried out on oxidized samples in 45 mM sodium phosphate buffer with 10% deuterium oxide at pH 7.0. The natural isotopic abundance NMR samples were prepared by oxidation of 3.0 mM *Ht* cyt c_{552} with 15 mM potassium ferricyanide ($K_3[Fe(CN)_6]$, Sigma), while the ^{13}C-enriched NMR samples contained 1–2 mM *Ht* cyt c_{552} and 10 mM $K_3[Fe(CN)_6]$. The protein concentrations were determined spectrophotometrically on a Shimadzu UV-2401 PC spectrophotometer using the extinction coefficient for WT *Ht* Fe(III)cyt c_{552} ($\varepsilon_{409.5\ nm}$ = 105 $mM^{-1}cm^{-1}$).26

All NMR spectra reported in this work were collected on a Varian Inova 500-MHz spectrometer equipped with a triple resonance probe. The NMR spectra of WT and A7F *Ht* cyt c_{552} were obtained at 51 °C, while the NMR spectra of the other four variants were obtained at 27 °C. The water signal was suppressed in all ^1H-detected NMR experiments using presaturation during the relaxation delay. ^1H-^{13}C heteronuclear multiple quantum coherence (HMQC)48 experiments for both natural isotopic abundance and 5-^{13}C-ALA *Ht* cyt c_{552} utilized a recycle time of 300 ms and a refocusing time of 2.5 ms (J_{CH} = 200 Hz). The ^1H-^1H two-dimensional nuclear Overhauser enhancement spectroscopy (NOESY) experiments with natural isotopic abundance samples used a recycle time of 1.2 s and a mixing time of 100 ms. ^{13}C-detected NMR spectra of the 5-^{13}C-ALA *Ht* cyt c_{552} samples, both with and without ^1H decoupling, were acquired with a relaxation delay of 20 ms. ^1H NMR spectra (2-s relaxation delay) collected immediately before and after every two-dimensional and ^{13}C-detected experiment were compared to verify sample integrity.

All one-dimensional NMR spectra were processed in MestRe-C with 10-Hz exponential line broadening, with the exception of the ^1H NMR spectra collected with a 2-s relaxation delay for which a 1-Hz line broadening was utilized.49 The two-dimensional NMR data were processed in NMRPipe with polynomial solvent correction of the time-domain data.50 Both dimensions of the ^1H-^{13}C HMQC data, which contained 2048 data points in the F2 dimension and either 512 (natural isotopic abundance samples) or 128 (5-^{13}C-ALA *Ht* cyt c_{552} samples) data points in the F1 dimension, were multiplied by a pure cosine-squared apodization function, zero-filled, and Fourier transformed to obtain 1024 × 2048 real data points. The raw, 2048 × 4096, ^1H-^1H NOESY data were also processed using a pure cosine-squared apodization function, zero-filling, and a Fourier transform to yield 2048 × 4096 real data points. Prior to the Fourier transform of the indirect (F1) dimension, forward linear prediction was used to double the number of data points in F1 for all two-dimensional NMR spectra. Lastly, a polynomial baseline correction was applied to both dimensions of the resulting square data matrix. NMRPipe processing scripts and fully processed NMR data are available in the Supporting Information.

All resonance assignments were made in Sparky,51 assisted by existing assignments for WT,26 Q64N,28 and Q64V *Ht* cyt c_{552}.29 The four intense peaks shifted far downfield in the ^1H dimension and far upfield in the ^{13}C dimension of the natural isotopic abundance ^1H-^{13}C HMQC spectrum were identified as the heme methyl resonances (Figure 2, 3).52 The identities of the heme meso ^1H and ^{13}C resonances were established using the ^1H-^{13}C HMQC spectrum of 5-^{13}C-ALA *Ht* cyt c_{552}.47 Specific resonance assignments were made using the ^1H-^1H NOESY cross-peaks between the heme methyl and meso ^1H resonances. For both Q64V and A7F/Q64V *Ht* cyt c_{552}, the α-meso ^1H resonance was obscured by the solvent signal and the ^{13}C resonance was instead identified in a 1-D ^{13}C NMR spectrum acquired without proton decoupling.53 The heme α-pyrrole ^{13}C resonances were deduced from the ^{13}C NMR spectra following assignment of the four heme meso carbons for each variant of *Ht* cyt c_{552}. The axial Met61 Cε^1H_3 resonance was identified in the ^1H NMR spectra as the only peak that integrated for three protons found upfield of −10

ppm.32 All resonance assignments made in this work are tabulated in the Supporting Information.

2.3. EPR Spectroscopy

The oxidized WT and A7F *Ht* cyt c_{552} EPR samples contained 500 μM *Ht* cyt c_{552} in 50 mM 4-(2-hydroxyethyl)-1-piperazineethanesulfonic acid (HEPES) buffer at pH 6.97. X-band (9.2 GHz) EPR spectra were acquired on a Bruker EMX spectrometer with the sample temperature maintained at 10 K by an Oxford ESR-10 continuous-flow liquid-helium cryostat. The EPR spectra were collected with 200 μW of microwave power, a 15 G field modulation at 100 kHz, and a time constant of 164 ms.

The SIMPOW6 program, which was developed by Dr. Mark Nilges at the University of Illinois based on the QPOW program,54 was used to simulate the EPR spectra and extract *g* values. The high-field *g* value of low-spin, Fe^{3+}hemes is often exceedingly difficult to observe and, consequently, the EPR simulations utilized the following normalization condition:

$$g_x^2+g_y^2+g_z^2+g_yg_z-g_xg_z-g_xg_y-4(g_z+g_y-g_x)=0 \quad (2)$$

that was previously derived using LFT.5,55 It is important to note that this equation assumes a $(d_{xy})^2(d_{xz,yz})^3$ electronic ground state and it will fail when there is significant mixture of other electron configurations into the ground state. The complete parameter sets for the EPR spectral simulations are available in the Supporting Information.

2.4. DFT Computations

The initial structural model for low-spin Fe^{3+}heme with His/Met axial ligation was derived from the X-ray crystal structure of WT *Ht* cyt c_{552} (PDB file 1YNR),27 which contains an axial Met in the *R* configuration. (In solution, the axial Met in WT *Ht* cyt c_{552} is fluxional). 22 All residues were removed with the exception of His16, Met61, and the heme cofactor. The His16 and Met61 residues were further trimmed by removing the peptide backbone nuclei and Cβ from each residue. The heme *c* cofactor was truncated by removing all nuclei more than one bond away from porphyrin π system. This resulting structural model is similar to one used previously to model cyt *c*,56 except the porphyrin ligand here is capped by eight methyl groups instead of eight hydrogens. To generate an initial structural model of Fe^{3+}heme with an axial Met ligand in the *S* configuration, the initial coordinates for Sδ and Cε of Met61 were replaced with those derived from the X-ray crystal structure of *Pa* cyt c_{551} (PDB file 351C),20 following alignment of all active site nuclei. All coordinate transformations, as well as the addition of hydrogen atoms, utilized ArgusLab graphical user interface.57

All electronic structure calculations presented in this work were carried out in the ORCA 2.6.35 software package on a 120 node IBM BladeCenter at the Center for Research Computing of the University of Rochester.58,59 The DFT calculations utilized the unrestricted Kohn-Sham formalism with tight SCF convergence criteria and a density functional composed of the Perdew-Wang 91 local density and the Perdew-Burke-Ernzerhof (PBE) generalized gradient functionals.60,61 While a previous DFT study of paramagnetic metallocenes has found that the accuracy of computed NMR shifts is improved by hybrid functionals,42 pure DFT has been found to be better at reproducing the complete active space SCF spin density of low-spin Fe(III)-porphyrin complexes.62 In addition, the resolution of the identity approximation can be used to speed up the calculation of the Coulomb term by approximating the molecule's charge distribution in pure DFT

calculations.63 For these reasons, we choose to use the PBE density functional with the TZV/J auxiliary basis set to model His/Met-ligated Fe^{3+}heme.64 The initial structural models were refined by a restricted geometry optimization of the $S = ½$ Fe^{3+}heme state with the TZVP basis set,65 where the heme(γ-meso)-Fe-His(Nε2)-His(Cε1) dihedral angle was constrained to the crystallographic value (1.5°), as was the heme(β-meso)-Fe-Met(Sδ)-Met(Cγ) dihedral angle (17.1° and −5.4° for the *R* and *S* Met configurations, respectively). These restraints were necessary to ensure that the axial ligand orientations dictated by the protein secondary structure were reproduced in the DFT model since both axial ligands have been shown to rotate freely and independently in Car-Parrinello trajectories of similar structural models of cyt *c*.66 Following these two restricted geometry optimizations, 11 additional Fe^{3+}heme geometries, with different amounts of heme ruffling, were generated for each axial Met configuration (*R* and *S*) using the TZVP basis set by constraining the dihedral angle between pyrrole rings B and D to a value between 10.0 and 30.0° in 2.0° increments, inspired by a strategy used in the past for metal-free and nickel poprhyrins.67,68 All dihedral angle constraints are identified graphically in the Supporting Information.69 The geometry optimizations used the following (standard to ORCA 2.6.35) convergence criteria: 0.000005 hartree change in total energy, 0.0001 hartree/Å in the Cartesian gradients, and 0.002 Å change in the Cartesian coordinates between subsequent cycles. The heme OOP distortion of each DFT-computed geometry was analyzed using the Normal-Coordinate Structural Decomposition procedure of Shelnutt and co-workers.2

The **g**, **A**(^{1}H), and **A**(^{13}C) tensors were calculated at each DFT-computed geometry using CP-SCF theory,43 with a complete mean-field treatment of spin-orbit coupling and the IGLO gauge origin.70 These CP-SCF calculations incorporated three contributions to the **A** tensor: the isotropic Fermi contact term, the spin-dipole term, and the second-order contribution from spin-orbit coupling. All CP-SCF calculations utilized the triply-polarized "Core Properties" (CP(PPP)) basis set on Fe and the IGLO-III basis set on all other nuclei.71,72 Following the calculation of the **g**, **A**(^{1}H), and **A**(^{13}C) tensors using CP-SCF theory, the $\boldsymbol{\sigma}_{HFS}$ tensors were calculated according to equation 1. The HFS observed by solution NMR spectroscopy corresponds to the isotropic portion of the $\boldsymbol{\sigma}_{HFS}$ tensor, which equals one-third times the trace of the $\boldsymbol{\sigma}_{HFS}$ tensor.

In addition, unrestricted single-point DFT calculations were performed for the Fe^{2+}heme state at all geometries optimized for the Fe^{3+}heme state using the TZVP basis set. A quasi-restricted orbital (QRO) analysis was applied to all DFT-computed electronic structures described in this work to aid their comparison.73 The frontier QROs, lowest-unoccupied spin-down MO, and unpaired spin densities were visualized with the gOpenMol program as isosurface plots using isodensity values of 0.025 and 0.0005 au, respectively.74–76 These isosurface plots are available in the Supporting Information.

3. Results and Analysis

3.1. NMR Spectroscopy

The primary goals of this work are to identify multiple ^{1}H and ^{13}C NMR spectroscopic observables that correlate with the magnitude of the heme ruffling OOP deformation and to determine the effect of this deformation on the electronic structure, and reactivity, of the heme cofactor. Previous studies on nitrophorins and model heme complexes indicate that the average heme methyl ^{1}H shift moves downfield as ruffling decreases.10,33 In this work, the A7F mutation is expected to decrease the amount of heme ruffling in *Ht* cyt c_{552}, based upon a comparison of the X-ray crystal structures of WT and F7A *Pa* cyt c_{551}, a closely related protein in which the variant with Phe at position 7 is less ruffled.20,21 If this proposal for *Ht* cyt c_{552} and its A7F mutant is correct, then the average heme methyl ^{1}H shift of oxidized *Ht* cyt c_{552} is expected to move downfield upon introduction of the A7F

mutation. The value of the average heme methyl ^{1}H shift is readily accessible via ^{1}H NMR spectroscopy (Figure 3), where four intense downfield peaks were previously assigned to the heme methyl ^{1}H resonances of WT *Ht* cyt c_{552}.26 The average shift is utilized to minimize effects of the axial ligand orientations and the local environment and to emphasize effects of heme OOP distortions on chemical shifts. Indeed, the average heme methyl ^{1}H shift moves downfield upon introduction of the A7F mutation (Table 1), which suggests that the A7F mutation decreases the amount of heme ruffling in *Ht* cyt c_{552} by comparison to other reports of this correlation.10,33 However, it is conceivable that this spectral change could be the result of a structural change other than ruffling in this particular case. Therefore, several additional differences between the NMR spectra of WT and A7F *Ht* cyt c_{552} will be identified and the consistency of these results with decreased ruffling in A7F *Ht* cyt c_{552} will be evaluated by comparison to the results of DFT calculations.

The heme methyl ^{13}C resonances also have the potential to monitor the ruffling OOP deformation because, like the heme methyl ^{1}H resonances, the spin density at these nuclei is ultimately derived from delocalization of the unpaired electron through the porphyrin π-system and onto the β-pyrrole carbons (Figure 2). Here, these ^{13}C resonances have been identified using their cross peaks with the heme methyl ^{1}H resonances in the ^{1}H-^{13}C HMQC spectrum of *Ht* cyt c_{552} (Figure 4). As was the case for the heme methyl ^{1}H resonances, the differences between the individual ^{13}C resonances are primarily a measure of the asymmetric distribution of spin density about the porphyrin ring, which is a consequence of interactions between the porphyrin π-system and the axial ligands.23 As a result, it is advantageous to average all four heme methyl ^{13}C resonances to minimize the contributions of the axial ligands and emphasize the contribution of OOP deformations. When these four ^{13}C shifts are averaged, the result is further upfield in the A7F variants of *Ht* cyt c_{552} and the magnitude of the observed change is larger than that observed for the ^{1}H resonances (Table 1).

The heme meso ^{1}H and ^{13}C resonances are intriguing as a potential NMR probe of the heme ruffling OOP deformation because the $(d_{xz,yz})^4(d_{xy})^1$ electron configuration stabilized by highly ruffled model complexes has positive spin density delocalized onto the meso carbons (Figure 2).33 Observation of the heme meso ^{1}H and ^{13}C resonances is challenging because these peaks are generally buried under the envelope of protein resonances, but the heme meso carbons can be selectively ^{13}C enriched if [5-^{13}C]-δ-aminolevulinic acid is used as the heme precursor during cofactor biosythesis.47 The heme meso resonances of the resultant 5-^{13}C-ALA *Ht* cyt c_{552} can be detected by ^{1}H-^{13}C HMQC spectroscopy (Figure 5).77 When the individual shifts are averaged to emphasize symmetric structural changes, the average heme meso ^{13}C and ^{1}H shifts move upfield in the A7F variants (Table 2).

Finally, a close examination of all the NMR spectroscopic data presented in this study identifies two additional NMR observables that show consistent changes upon introduction of the A7F mutation. First, the Met C$\varepsilon^{1}H_3$ resonance, which can be identified in the ^{1}H NMR spectrum of *Ht* cyt c_{552} (Figure 3), shifts upfield in A7F *Ht* cyt c_{552} (Table 3). Second, the average ^{13}C shift of the four heme α-pyrrole carbons enriched in 5-^{13}C-ALA *Ht* cyt c_{552} (Figure 2),47 which can be determined from a 1-D ^{13}C NMR spectrum following assignment of the heme meso ^{13}C resonances (Figure 6), moves upfield upon introduction of the A7F mutation (Table 3).

Once sets of heme methyl and meso ^{1}H resonances for *Ht* cyt c_{552} were identified, specific ^{1}H resonance assignments were made using ^{1}H-^{1}H NOESY spectroscopy. The ^{1}H resonance assignments were used to make specific ^{13}C resonance assignments based upon the observed cross peaks in the ^{1}H-^{13}C HMQC data (Figures 4 and 5). The resulting heme methyl ^{1}H shift patterns confirmed the proposal that the identity of residue 64 controls the

axial Met configuration in *Ht* cyt c_{552}.22,23 Indeed, the configuration of the axial Met is best described as *S* in variants containing Asn64, *R* in variants containing Val64, and fluxional in variants containing the native Gln64. Importantly, all of the observed A7F-induced spectral changes are insensitive to the axial Met configuration (Tables 1–3). This strongly suggests that the process of averaging the heme methyl and meso HFSs minimizes contributions from changes to the axial ligand orientations. A complete tabulation of the heme ^{1}H and ^{13}C resonance assignments described here is available in the Supporting Information.

Characterizing the relationship between the heme ruffling OOP deformation and the electronic structure and function of the heme cofactor will ultimately inspire the use of DFT computations, but some information can be derived from the results of NMR spectroscopy alone. In paramagnetic systems, the observed chemical shift has two major components: the diamagnetic shift, which should be nearly equal to the chemical shift in Fe(II) (*S* = 0) cyt *c*, 78 and the HFS. The average heme methyl ^{1}H shift for reduced *Ht* cyt c_{552} is 3.65,25 the average heme methyl ^{13}C shift for reduced horse cyt *c* is 14.7 ppm,32 and the α-pyrrole shifts in reduced cyt *c* are almost certainly greater than +100 ppm since these carbons are part of an aromatic system. Thus, the heme methyl ^{1}H resonances experience a positive HFS, whereas the heme methyl and α-pyrrole ^{13}C resonances have negative HFSs in cyt *c* (Tables 1 and 3). The signs of these HFSs are all consistent with a spin polarization mechanism where positive spin density on the β-pyrrole carbons is transferred to the surrounding nuclei with a sign reversal for each σ-bond.79 Furthermore, the increase of the ^{1}H and ^{13}C HFSs in A7F *Ht* cyt c_{552} relative to WT *Ht* cyt c_{552} suggests that the A7F mutation increases this positive spin density on the β-pyrrole carbons (Table 1).

In contrast, the sign of the average heme meso ^{13}C HFS cannot be explained by spin polarization from positive spin density on the β-pyrrole carbons. If this were the primary contribution to the NMR HFS of the heme meso ^{13}C resonances, then the sign would be positive.79 Instead, based on the average heme meso ^{13}C shift of reduced horse heart cyt *c* (97.4 ppm),80 the sign of the heme meso ^{13}C HFS is negative (Table 2). Importantly, negative spin density at the meso carbons of a low-spin porphyrin-imidazole complexes has been observed previously,81 and is a consequence of electron correlation. Furthermore, the observed effect of the A7F mutation on the average heme meso ^{13}C HFS of *Ht* cyt c_{552} suggests that the negative spin density increases upon introduction of the A7F mutation.

3.2. EPR Spectroscopy

The NMR spectroscopic probes identified above have helped elucidate the spatial distribution of the HOMO in *Ht* cyt c_{552}, and its response to the A7F mutation, but EPR spectroscopy is better suited to monitor the relative energies of the Fe 3*d*-based MOs.37 Taylor has developed a LFT-based method to calculate the relative energies of the Fe $3d_{xy}$-, $3d_{xz}$-, and $3d_{yz}$-orbitals from the *g* values measured by EPR under the assumption that the HOMO can be described exclusively in terms of these three Fe 3*d*-orbitals.55 In this method, the measured *g* values determine a rhombic term (V/ξ) and an axial term (Δ/ξ); together, these two terms describe the relative energies of the Fe $3d_{xy}$-, $3d_{xz}$-, and $3d_{yz}$-orbitals. Furthermore, this method describes the HOMO as a linear combination of these three Fe 3*d*-orbitals, whose relative contributions are determined by coefficients derived from the EPR *g* values. Consequently, once the *g* values are extracted from the EPR spectra of *Ht* cyt c_{552}, the relative energies of the three occupied Fe 3*d*-orbitals and a description of HOMO can be deduced using Taylor's LFT-based method.

A comparison of the X-band EPR spectra of oxidized WT and A7F *Ht* cyt c_{552} allows the influence of the A7F mutation on the relative energies of the Fe 3*d*-based MOs to be established (Figure 7). The differences between the *g* values and LFT terms extracted from

the EPR spectra of WT and A7F *Ht* cyt c_{552} are small (Table 4).55 The axial ligand field parameter may be slightly larger in A7F *Ht* cyt c_{552}, although the observed change is smaller than experimental error. An increase in Δ/ξ would be consistent with preferential stabilization of the Fe $3d_{xy}$-orbital, in accord with decreased ruffling upon introduction of the A7F mutation.5 The LFT-based analysis also indicates that the overall description of the HOMO in *Ht* cyt c_{552} is relatively unchanged by the A7F mutation. Most importantly, the contribution of the Fe $3d_{xy}$-orbital to the HOMO is extremely small (~2%) in both WT and A7F *Ht* cyt c_{552}. This indicates that the ruffling-induced electronic structure changes observed in cyt *c* are fundamentally different from the $(d_{xy})^2(d_{xz,yz})^3$ to $(d_{xz,yz})^4(d_{xy})^1$ electron configuration change observed in model complexes upon the introduction strong π-acceptor axial ligands.33,34

3.3. DFT Computations

DFT computations complement the NMR and EPR data presented above in three major ways. First, the complete electronic structure of His/Met-ligated heme is predicted by a DFT calculation, whereas only the portion of the electronic structure that contributes to the observed spectrum can be inferred from spectroscopic data alone. Second, it is possible to monitor the influence of one geometric deformation (e.g. ruffling) on the electron and spin density of the cofactor in the near complete absence of other distortions using theory, which is exceedingly difficult to achieve in an experiment. Finally, theoretical calculations are capable of predicting results not yet observed experimentally, such as additional spectroscopic probes of heme ruffling and the implications of the ruffling OOP deformation with respect to the electron transfer properties of cyt *c*. However, while DFT represents a good compromise between computational efficiency and a reasonable approximation to electron correlation, the validity of the approximations inherent to a given choice of density functional and basis set for His/Met-ligated heme must be assessed by comparison to spectroscopic data. In this study, we will assume that if this electronic structure can accurately predict the observed spectroscopic data, then the underlying DFT-computed electronic structure is also accurate and we can interpret the predictions of DFT with confidence.

Electronic structure descriptions for oxidized His/Met-ligated heme, with the axial Met in either the *R* or *S* configuration, were generated at several points along a ruffling coordinate using the PBE density functional and the TZVP basis set.61,65 The three occupied PBE DFT-computed Fe 3*d*-based MOs for His/Met-ligated heme (*R* Met) are shown in Figure 8. All three occupied Fe 3*d*-based MOs are partially delocalized onto the porphyrin ligand as a consequence of anti-bonding interactions; the Fe $3d_{xy}$-orbital mixes with a porphyrin π-orbital that has a_{2u} symmetry in the D_{4h} point group, while the $3d_{xz}$- and $3d_{yz}$-orbitals mix with a set of porphyrin π* orbitals with e_g symmetry. In addition, the Fe $3d_{xz}$- and $3d_{yz}$-orbitals also mix with the His imidazole π-system and the Met sulfur lone pair. When the axial Met configuration is changed from *R* to *S*, the computed Fe 3*d*-based MOs are nearly identical except that the re-orientation of the axial Met lone pair causes the energies of the Fe $3d_{xz}$- and Fe $3d_{yz}$-based MOs to be interchanged.

In the low-spin, d^5 electron configuration of oxidized cyt *c* (*R* Met), the Fe $3d_{xz}$-based MO is singly-occupied by a spin-up electron resulting in the positive spin density shown in red (Figure 8). When the axial Met configuration is *S*, the interchange of the Fe $3d_{xz}$- and $3d_{yz}$-based MO energies induces an approximate 90° rotation of the positive spin density. The PBE DFT-computed spin densities for both isomers are in accord with the observed heme methyl ^{1}H and ^{13}C HFS data for Q64N and Q64V *Ht* cyt c_{552}. The negative spin density shown in gray on the Fe-ligating atoms predicted by DFT for both isomers is strange at first glance because, formally, there are no unpaired spin-down electrons in low-spin Fe(III). However, negative spin density has been reported before for low-spin porphyrins,82 and it

arises from two quantum mechanical considerations.83 First, the exchange energy associated with the triply-occupied spin-up Fe 3*d*-orbitals is more negative than that of the doubly-occupied spin-down 3*d*-orbitals, which results in ligand-to-metal electron donation similar in nature to the DFT-predicted electronic reorganization of bis-His heme upon reduction.84 Second, the spin-down density in the regions with diminished spin-up density (a consequence of the porphyrin-to-Fe electron donation in the spin-up manifold) increases because the correlation energy penalty associated with bringing two electrons close together is diminished.

To assess the accuracy of the PBE DFT-computed positive spin densities arising from the unpaired electron formally assigned to either the Fe $3d_{xz}$- or $3d_{yz}$-based MO, the heme methyl ^{13}C and ^{1}H HFSs were calculated at each point along the computed ruffling coordinate using equation 1 (Figure 8). Since the NMR HFS depends exclusively on the portion of the spin density found at the nucleus,31 basis sets with flexible descriptions of the core orbitals were used to calculate the **A**-tensors with CP-SCF theory. The valence MO and spin density descriptions predicted with the flexible core basis sets were nearly identical to those predicted with the TZVP basis set, which implies that heme methyl ^{13}C and ^{1}H HFSs computed with flexible core basis sets are a reasonable test of the Fe $3d_{xz}$- and $3d_{yz}$-based MO descriptions described above. Recall that the average heme methyl ^{13}C and ^{1}H HFSs of *Ht* cyt c_{552} are negative and positive, respectively (Figures 3 and 4 and Table 1), and the sizes of these HFSs increase when the A7F mutation is introduced. If the A7F mutation decreases the magnitude of the heme ruffling OOP deformation, then the signs of the PBE DFT-computed average heme methyl ^{13}C and ^{1}H HFSs, as well as the qualitative changes induced by ruffling, are in agreement with the NMR results. In addition, Löwdin population analysis of the DFT-computed electronic structure also confirms the proposal that positive spin density on the β-pyrrole carbons, and its decrease with increased heme ruffling, is responsible for the observed heme methyl NMR HFS data, as the PBE DFT-computed positive spin density on these carbons decreases by 10% across the 0.6 Å range probed computationally. As a consequence of the excellent agreement between the DFT-predicted heme methyl ^{13}C and ^{1}H HFS data and the NMR results for *Ht* cyt c_{552}, the spatial distribution and ruffling response of the PBE DFT Fe $3d_{xz}$- and $3d_{yz}$-based MOs can be trusted and interpreted.

The accuracy of the PBE DFT-predicted Fe $3d_{xy}$-based MO was assessed by comparison of the experimental and theoretical average heme meso ^{13}C and ^{1}H HFSs. The sign of the DFT-computed average heme meso ^{13}C HFS and the small ^{1}H HFS both agree with the experimental NMR data (Table 2). Specifically, for A7F compared to wild-type, the observed average ^{13}C shift decreases, consistent with a more negative ^{13}C HFS in the more planar heme. Löwdin population analysis indicates that while the negative spin density on the heme meso carbons at the DFT-optimized geometry is five-times smaller than the positive spin density on β-pyrrole carbons, this negative spin density is quite sensitive to the ruffling OOP deformation, decreasing by over 90% across the 0.6-Å range probed computationally. Finally, the PBE DFT-computed heme α-pyrrole ^{13}C HFSs and Met Cε ^{1}H HFSs, along with their responses to increased heme ruffling, agree with the experimental data for *Ht* cyt c_{552} if A7F *Ht* cyt c_{552} is less ruffled than WT (Figure 8 and Table 3). Together, the excellent agreement between the experimental NMR data and the theoretical results strongly suggest that the A7F mutation decreases heme ruffling in *Ht* cyt c_{552}. Also, the agreement between theory and experiment confirms the accuracy of the PBE DFT-computed spin density distributions and Fe 3*d*-based MO descriptions, along with the overall decrease in spin delocalization from the Fe center in ruffled hemes.

The accuracies of the PBE DFT-computed Fe 3*d*-orbital energies can be better evaluated using the experimental EPR data rather than the NMR data. Unfortunately, the observed *g*

shifts in WT and A7F *Ht* cyt c_{552} are too large to be realistically modeled by a perturbation theory-based method (Figure 7), such as CP-SCF.43 Nevertheless, the energies of the PBE DFT-computed Fe 3*d*-based MOs can be compared to the LFT terms extracted from the EPR spectra of *Ht* cyt c_{552} (Table 4).55 The energies of all three occupied Fe 3*d*-based MOs, both for the Fe(III) and the Fe(II) states, increase almost linearly with ruffling of the cofactor. The PBE DFT-computed Fe $3d_{xy}$-based MO is the most destabilized, which would be consistent with a decreased Δ/ξ as ruffling increases. In the present study, changes in EPR spectra as a function of ruffling are very small, but the computational results suggest that greater changes in ruffling and more ruffled systems may exhibit significant changes LFT parameters extracted from EPR spectra. A more detailed environmental model would be required to interpret detailed local changes of the cofactor arising from the mixing of the nearly degenerate Fe $3d_{xz}$- and Fe $3d_{yz}$-based MOs. The environment of the cofactor also introduces additional asymmetry into the spin density distribution and NMR HFSs that can be partially accounted for by including the side-chains of the cofactor in the computational model (Table S12).

4. Discussion

4.1. NMR Probes of Heme Ruffling

Several spectroscopic measures of the heme OOP ruffling deformation are established in this work. Previous research has established that the average heme methyl ^{1}H NMR shift of oxidized heme moves upfield with increased heme ruffling (Figure 9). In addition, four new NMR spectroscopic probes of the ruffling OOP deformation of heme with the $(d_{xy})^2(d_{xz,yz})^3$ configuration have been identified in this work by virtue of agreement between the observed NMR spectral changes of WT, Q64N, and Q64V *Ht* cyt c_{552} upon introduction of the A7F mutation and the DFT-computed changes predicted for a ruffling deformation of heme. While it is possible that agreement between theory and experiment could be accidental for one data point, it is extremely unlikely that five different data points for three different sets of protein variants would agree with theoretical predictions by chance. Both the NMR data and the DFT calculations suggest that the average heme methyl and meso ^{13}C HFSs are even more sensitive probes of increased heme ruffling than the average heme methyl ^{1}H shift (Scheme 1). Again, it is important to point out the importance of averaging the NMR shifts to emphasize the contributions of ruffling to the measured data. The “average” heme α-pyrrole ^{13}C shift and the Met Cε^1H$_3$ shift are also identified as measures of the heme OOP deformation based upon agreement between theory and experiment, but both of these results require further comment. DFT calculations suggest that the average ^{13}C HFS of all eight heme α-pyrrole carbons is an excellent, near linear, measure of heme ruffling, but measurement of all eight heme α-pyrrole ^{13}C NMR shifts would require additional ^{13}C-enrichment of the cofactor.47 The Met Cε^1H$_3$ HFS, along with any other axial ligand HFS, should be interpreted with caution because any observed changes could also be a consequence of stronger or weaker axial ligand bonding interactions.85

It is informative to predict the magnitude of the heme ruffling OOP deformation in A7F *Ht* cyt c_{552} as an illustration of the predictive potential of NMR spectroscopic data when interpreted within the DFT framework presented here. First, we will assume that the 0.62 Å heme ruffling observed in the X-ray crystal structure of WT *Ht* cyt c_{552} is an accurate representation of the equilibrium solution structure of the cofactor at 51 °C and that the axial Met configuration in WT and A7F *Ht* cyt c_{552} is an equal mixture of *R* and *S* Met.27 Based upon the DFT-predicted average heme methyl ^{1}H HFS (Figure 9), the 0.17 ppm downfield shift observed in A7F *Ht* cyt c_{552}, relative to WT (Table 1), is consistent with a 0.05 Å flattening of the porphyrin ring. Similarly, the heme methyl and meso ^{13}C HFS data are consistent with 0.16 and 0.05 Å decreases of heme ruffling in the mutant, respectively (Tables 1 and 2, Figure 9). The variability of the structural change predicted by these three

correlations emphasizes the importance of identifying several NMR probes of heme ruffling. Each NMR probe of ruffling likely has its own specific shortcomings derived from the contributions of other structural and environmental changes in the system. Only critical comparison with the NMR HFS data from future studies will identify the "best" NMR probe or probes of heme ruffling. Importantly, the 0.46-to-0.57 Å ruffling predicted here for A7F *Ht* cyt c_{552} is consistent with the 0.49 Å ruffling of the heme cofactor in the X-ray crystal structure of WT *Pa* cyt c_{551},20 which also has a phenylalanine at position 7.

4.2. Electronic Structure of Low-Spin Heme with His/Met Axial Ligation

Theoretical models of porphyrin electronic structure date back over 50 years to Gouterman,86 but the agreement of the DFT-predicted Fe 3*d*-based MO electronic structure presented in this work with the NMR and EPR spectral data is the most comprehensive to date for His/Met-ligated heme. Importantly, the Fe $3d_{xz}$- and $3d_{yz}$-based MO descriptions are similar to those in Walker's Hückel theory model (Figure 8),23 which has proven to be extremely successful at correlating the positive spin density distribution onto the heme methyl and meso protons with the orientation(s) of the axial ligands. Furthermore, the additional porphyrin-to-Fe electron transfer in the spin-down Fe $3d_{xy}$-based MO relative to its spin-up counterpart has some precedent, as negative spin density on the heme meso carbons of low-spin porphyrin complexes has been reported previously.81,82 However, a realistic treatment of the local changes to the electronic structure introduced by the asymmetric environment of the protein secondary structure and the low-lying electronic excited state known to exist for cyts *c*32 are a prerequisite to future efforts to interpret geometric and electronic changes of the heme cofactor at an atomic level of detail. Yet, for now, the real novelty of the DFT-predicted Fe 3*d*-based MO electronic structure presented here is its understanding of the electronic, spectroscopic, and functional consequences of the ruffling OOP deformation of heme.

The PBE DFT calculations indicate that the ruffling OOP deformation introduces several changes to the electronic structure of low-spin, His/Met-ligated heme and a careful analysis of the results provides a rationale for these changes. First, the DFT calculations indicate that the positive spin density on the β-pyrrole carbons decreases as a function of heme ruffling, which is supported by the *Ht* cyt c_{552} heme methyl ^{13}C and ^{1}H NMR data (Table 1). The reason there is less positive spin density delocalized onto the β-pyrrole carbons is that the ruffling deformation reduces the orbital overlap between the Fe $3d_{\pi}$ and the pyrrole $2p_z$ orbitals. In addition, the DFT results suggest, and the heme meso ^{13}C NMR data confirm (Table 2), that the negative spin density found on the heme meso carbons decreases in ruffled hemes. However, unlike highly ruffled heme model complexes with strong π-acceptor axial ligands,33 this is not due to delocalization of the unpaired (spin-up) electron onto the meso carbons. Instead, the ruffling deformation increases the Fe $3d_{\pi}$-based electron density on the Fe center, which makes heme meso-to-Fe $3d_{xy}$ electron donation less energetically favorable. Finally, the DFT calculations indicate that all three occupied Fe 3*d*-based MOs are destabilized by the ruffling OOP deformation with the Fe $3d_{xy}$-based MO being the most sensitive to ruffling, in agreement with the *Ht* cyt c_{552} EPR data (Table 4). The destabilization of the Fe $3d_{xy}$-based MO is the result of increased anti-bonding character with the occupied porphyrin $\pi(a_{2u})$ orbital as a consequence of increased overlap in ruffled hemes. Alternatively, the destabilization of the Fe $3d_{xz}$- and $3d_{yz}$-based MOs are due to decreased overlap with the unoccupied porphyrin $\pi^*(e_g)$ orbitals, which reduces the stabilizing π-backbonding interaction.

It is important to emphasize here that the ruffling OOP deformation does not change the electronic ground state of Fe(III) heme in cyt *c*. This indicates that the ground state electron configuration change from $(d_{xy})^2(d_{xz,yz})^3$ to $(d_{xz,yz})^4(d_{xy})^1$ observed in ruffled model complexes with strong π-acceptor axial ligands can be attributed to the nature of the axial

ligands rather than the heme ruffling.33,34 In these model complexes, the π-acceptor ligands stabilize the Fe $3d_{xz}$- and $3d_{yz}$-based MOs to the point that the Fe $3d_{xy}$-based MO becomes the singly-occupied MO, which favors heme ruffling. In contrast, the data presented here demonstrates that this mechanism for changing the electronic ground state of Fe(III) heme is not operative with the axial ligand set found in cyts *c*. This highlights the importance of selection of axial ligand set when modeling the geometric and electronic structure of heme proteins.

4.3. Implications for Fe(III) to Fe(II) reduction for His/Met-ligated heme

Marcus theory states that the rate of electron transfer depends on the driving force, the reorganization energy, and the electronic coupling of the donor and acceptor.87 The electronic coupling is the only term with directional implications; this term depends on the overlap integral of the donor MO describing the electron to be transferred and the acceptor MO describing the electron hole. When Fe(III) heme acts as an electron acceptor, the electron hole is described by the lowest unoccupied spin-down molecular orbital. In cyt *c*, this molecular orbital is well-described by the spin-up density because all electrons are paired in the reduced, Fe(II) heme, state (Figure 8 and S36). Therefore, the electronic coupling of His/Met-ligated heme with an external reductant that approaches the solvent-exposed edge of the cofactor is largest in the direction of the β-pyrrole carbons with large positive spin densities. The decreased delocalization of the Fe $3d_{\pi}$-based MOs onto the β-pyrrole carbons in ruffled hemes diminishes the value of the overlap integral at the β-pyrrole carbons. Furthermore, in contrast to heme model complexes with strong π-acceptor axial ligands,33 the value of the overlap integral at the heme meso carbons in His/Met-ligated heme is negligible regardless of the magnitude of the ruffling OOP deformation. The environment of the cofactor including its substituents and the active site residues will influence the spin density distribution and electron transfer pathway, but, in the absence of other considerations, the rate of electron transfer from an external reductant to cyt *c* should decrease as ruffling localizes the electron hole on the buried Fe center.

However, DFT calculations of His/Met-ligated heme imply that, in addition to decreasing the electronic coupling of the cofactor with an external reductant, the ruffling OOP deformation also modifies the reduction potential of the heme. As discussed above, all three occupied Fe 3*d*-based MOs are destabilized by heme ruffling in the DFT-computed electronic structures of Fe(III) and Fe(II) heme. Since these three MOs are occupied by six electrons in Fe(II) heme and only five in Fe(III) heme, the Fe(II) heme state should be preferentially destabilized by increased ruffling, which lowers the reduction potential of Fe(III) heme. Indeed, the increase of the total electronic energy as a function of the heme ruffling OOP deformation is steeper for the Fe(II) state as compared to the Fe(III) state. This DFT-predicted decrease of the heme reduction potential in response to increased ruffling is in accord with the measured decrease of the *Pa* cyt c_{551} reduction potential by about 100 mV in the more ruffled F7A variant relative to WT.20,21,88 The prediction also agrees with the correlation between the heme ruffling OOP deformation and the reduction potentials of the individual hemes in cyts c_3.89 This DFT-based prediction that the ruffling OOP deformation can alter two terms in the Marcus equation,87 the electronic coupling and the heme reduction potential, suggests that the modification of the magnitude of heme ruffling by the protein environment may be utilized in nature to optimize the rate of electron transfer between His/Met-ligated heme and a redox partner.

Supplementary Material

Refer to Web version on PubMed Central for supplementary material.

Acknowledgments

This work was supported by the NIH (GM63170 to K.L.B. and F32 GM089016 to M.D.L.). We acknowledge Dr. Boris Dzikovski and the National Biomedical Research Center for AdvanCed ESR Technology at Cornell, which is supported by Grant Number 5P41RR016292 from the National Center for Research Resources (NCRR), a component of the National Institutes of Health (NIH), for access to X-band EPR instrumentation as well as assistance with data collection. We also acknowledge the University of Rochester Center for Research Computing, Prof. Frank Neese (Universität Bonn) for providing the ORCA 2.6.35 software package, and Prof. Mark Nilges and the Illinois EPR Research Center for providing a copy of the SIMPOW6 program. Finally, we thank Prof. Marcel Swart (Universitat de Girona) for critically reading an earlier version of this manuscript.

References

1. Shelnutt JA, Song XZ, Ma JG, Jia SL, Jentzen W, Medforth CJ. Chem. Soc. Rev. 1998; 27:31–41.
2. Jentzen W, Song XZ, Shelnutt JA. J. Phys. Chem. B. 1997; 101:1684–1699.
3. Jentzen W, Ma JG, Shelnutt JA. Biophys. J. 1998; 74:753–763. [PubMed: 9533688]
4. Hobbs JD, Shelnutt JA. J. Protein Chem. 1995; 14:19–25. [PubMed: 7779259]
5. Zoppellaro G, Harbitz E, Kaur R, Ensign AA, Bren KL, Andersson KK. J. Am. Chem. Soc. 2008; 130:15348–15360. [PubMed: 18947229]
6. Hagarman A, Wallace CJ, Laberge MM, Schweitzer-Stenner R. J. Raman Spectrosc. 2008; 39:1848–1858.
7. Rivera M, Caignan GA, Astashkin AV, Raitsimring AM, Shokhireva TK, Walker FA. J. Am. Chem. Soc. 2002; 124:6077–6089. [PubMed: 12022842]
8. Lee WC, Reniere ML, Skaar EP, Murphy MEP. J. Biol. Chem. 2008; 283:30957–30963. [PubMed: 18713745]
9. Kubo M, Gruia F, Benabbas A, Barabanschikov A, Montfort WR, Maes EM, Champion PM. J. Am. Chem. Soc. 2008; 130:9800–9811. [PubMed: 18597456]
10. Shokhireva TK, Shokhirev NV, Berry RE, Zhang HJ, Walker FA. J. Biol. Inorg. Chem. 2008; 13:941–959. [PubMed: 18458965]
11. Yang F, Knipp M, Shokhireva TK, Berry RE, Zhang HJ, Walker FA. J. Biol. Inorg. Chem. 2009; 14:1077–1095. [PubMed: 19517143]
12. Tran R, Boon EM, Marletta MA, Mathies RA. Biochemistry. 2009; 48:8568–8577. [PubMed: 19653642]
13. Pauleta SR, Lu Y, Goodhew CF, Moura I, Pettigrew GW, Shelnutt JA. Biochemistry. 2008; 47:5841–5850. [PubMed: 18442258]
14. Gruia F, Kubo M, Ye X, Ionascu D, Lu C, Poole RK, Yeh SR, Champion PM. J. Am. Chem. Soc. 2008; 130:5231–5244. [PubMed: 18355013]
15. Shokhireva TK, Berry RE, Uno E, Balfour CA, Zhang HJ, Walker FA. Proc. Natl. Acad. Sci. U.S.A. 2003; 100:3778–3783. [PubMed: 12642672]
16. Ionascu D, Gruia F, Ye X, Yu AC, Rosca F, Beck C, Demidov A, Olson JS, Champion PM. J. Am. Chem. Soc. 2005; 127:16921–16934. [PubMed: 16316238]
17. Benning MM, Wesenberg G, Caffrey MS, Bartsch RG, Meyer TE, Cusanovich MA, Rayment I, Holden HM. J. Mol. Biol. 1991; 220:673–685. [PubMed: 1651396]
18. Bowman SEJ, Bren KL. Nat. Prod. Rep. 2008; 25:1118–1130. [PubMed: 19030605]
19. Ma JG, Laberge M, Song XZ, Jentzen W, Jia SL, Zhang J, Vanderkooi JM, Shelnutt JA. Biochemistry. 1998; 37:5118–5128. [PubMed: 9548742]
20. Matsuura Y, Takano T, Dickerson RE. J. Mol. Biol. 1982; 156:389–409. [PubMed: 6283101]
21. Borgia A, Bonivento D, Travaglini-Allocatelli C, Di Matteo A, Brunori M. J. Biol. Chem. 2006; 281:9331–9336. [PubMed: 16452476]
22. Zhong LH, Wen X, Rabinowitz TM, Russell BS, Karan EF, Bren KL. Proc. Natl. Acad. Sci. U.S.A. 2004; 101:8637–8642. [PubMed: 15161973]
23. Shokhirev NV, Walker FA. J. Biol. Inorg. Chem. 1998; 3:581–594.
24. Senn H, Keller RM, Wüthrich K. Biochem. Biophys. Res. Commun. 1980; 92:1362–1369. [PubMed: 6245651]

25. Hasegawa J, Yoshida T, Yamazaki T, Sambongi Y, Yu YH, Igarashi Y, Kodama T, Yamazaki K, Kyogoku Y, Kobayashi Y. Biochemistry. 1998; 37:9641–9649. [PubMed: 9657676]
26. Karan EF, Russell BS, Bren KL. J. Biol. Inorg. Chem. 2002; 7:260–272. [PubMed: 11935350]
27. Travaglini-Allocatelli C, Gianni S, Dubey VK, Borgia A, Di Matteo A, Bonivento D, Cutruzzola F, Bren KL, Brunori M. J. Biol. Chem. 2005; 280:25729–25734. [PubMed: 15883159]
28. Wen X, Bren KL. Biochemistry. 2005; 44:5225–5233. [PubMed: 15794659]
29. Bowman SEJ. Private communication.
30. Takayama SJ, Takahashi Y, Mikami S, Irie K, Kawano S, Yamamoto Y, Hemmi H, Kitahara R, Yokoyama S, Akasaka K. Biochemistry. 2007; 46:9215–9224. [PubMed: 17658890]
31. Bertini, I.; Luchinat, C.; Parigi, G. Solution NMR of Paramagnetic Molecules: Application to Metallobiomolecules and Models. Vol. Vol. 2. Amsterdam, The Netherlands: Elsevier; 2001.
32. Banci L, Bertini I, Luchinat C, Pierattelli R, Shokhirev NV, Walker FA. J. Am. Chem. Soc. 1998; 120:8472–8479.
33. Nakamura M. Coord. Chem. Rev. 2006; 250:2271–2294.
34. Rath SP, Olmstead MM, Balch AL. Inorg. Chem. 2006; 45:6083–6093. [PubMed: 16842017]
35. Shokhireva TK, Weichsel A, Smith KM, Berry RE, Shokhirev NV, Balfour CA, Zhang HJ, Montfort WR, Walker FA. Inorg. Chem. 2007; 46:2041–2056. [PubMed: 17290983]
36. Cai S, Shokhireva TK, Lichtenberger DL, Walker FA. Inorg. Chem. 2006; 45:3519–3531. [PubMed: 16634582]
37. Walker FA. Coord. Chem. Rev. 1999; 185–6:471–534.
38. Palmer, G. Physical Methods in Bioinorganic Chemistry: Spectroscopy and Magnetism. Que, L., editor. Sausalito, CA: University Science Books; 2000. p. 121-185.
39. Mao J, Zhang Y, Oldfield E. J. Am. Chem. Soc. 2002; 124:13911–13920. [PubMed: 12431123]
40. Machonkin TE, Westler WM, Markley JL. Inorg. Chem. 2005; 44:779–797. [PubMed: 15859246]
41. Moon, S.; Patchkovskii, S. Calculation of NMR and EPR Parameters. Theory and Applications. Kaupp, M.; Bühl, M.; Malkin, VG., editors. Weinheim, Germany: Wiley; 2004.
42. Hrobarik P, Reviakine R, Arbuznikov AV, Malkina OL, Malkin VG, Kohler FH, Kaupp M. Journal of Chemical Physics. 2007; 126
43. Neese F. J. Chem. Phys. 115:11080–11096.
44. Fee JA, Chen Y, Todaro TR, Bren KL, Patel KM, Hill MG, Gomez-Moran E, Loehr TM, Ai JY, Thöny-Meyer L, Williams PA, Stura E, Sridhar V, McRee DE. Protein Sci. 2000; 9:2074–2084. [PubMed: 11152119]
45. Ho SN, Hunt HD, Horton RM, Pullen JK, Pease LR. Gene. 1989; 77:51–59. [PubMed: 2744487]
46. Arslan E, Schulz H, Zufferey R, Kunzler P, Thöny-Meyer L. Biochem. Biophys. Res. Commun. 1998; 251:744–747. [PubMed: 9790980]
47. Alontaga AY, Bunce RA, Wilks A, Rivera M. Inorg. Chem. 2006; 45:8876–8881. [PubMed: 17054345]
48. Müller L. J. Am. Chem. Soc. 1979; 101:4481–4484.
49. Cobas JC, Sardina FJ. Concepts Magn. Reson. Part A. 2003; 19A:80–96.
50. Delaglio F, Grzesiek S, Vuister GW, Zhu G, Pfeifer J, Bax A. J. Biomol. NMR. 1995; 6:277–293. [PubMed: 8520220]
51. Goddard, TD.; Kneller, DG. Sparky 3. San Francisco: University of California;
52. Santos H, Turner DL. FEBS Lett. 1986; 194:73–77. [PubMed: 3000825]
53. In a 1-D 13C NMR spectrum of 5-13C-ALA Ht cyt c552, four of the eight 13C resonances split into doublets when 1H decoupling is turned off. These are the heme meso 13C resonances.
54. Nilges, MJ. Ph.D. thesis. Urbana, IL: University of Illinois; 1979.
55. Taylor CPS. Biochim. Biophys. Acta. 1977; 491:137–149. [PubMed: 191085]
56. Rovira C, Carloni P, Parrinello M. J. Phys. Chem. B. 1999; 103:7031–7035.
57. Thompson, MA. ArgusLab 4.0.1. Seattle, WA: Planaria Software LLC; http://www.arguslab.com.
58. Neese, F. ORCA 2.6.35. Bonn, Germany: Universität Bonn; 2008.
59. Neese F. Coord. Chem. Rev. 2009; 253:526–563.

60. Perdew JP, Wang Y. Phys. Rev. B. 1992; 45:13244–13249.
61. Perdew JP, Burke K, Ernzerhof M. Phys. Rev. Lett. 1996; 77:3865–3868. [PubMed: 10062328]
62. Radon M, Broclawik E, Pierloot K. J. Phys. Chem. B. 2010; 114:1518–1528. [PubMed: 20047294]
63. Neese F. J. Comput. Chem. 2003; 24:1740–1747. [PubMed: 12964192]
64. Eichkorn K, Weigend F, Treutler O, Ahlrichs R. Theor. Chem. Acc. 1997; 97:119–124.
65. Schafer A, Horn H, Ahlrichs R. Journal of Chemical Physics. 1992; 97:2571–2577.
66. Furlan S, La Penna G, Banci L, Mealli C. J. Phys. Chem. B. 2007; 111:1157–1164. [PubMed: 17266270]
67. Wertsching AK, Koch AS, DiMagno SG. J. Am. Chem. Soc. 2001; 123:3932–3939. [PubMed: 11457143]
68. Haddad RE, Gazeau S, Pécaut J, Marchon J-C, Medforth CJ, Shelnutt JA. J. Am. Chem. Soc. 2003; 125:1253–1268. [PubMed: 12553827]
69. For geometries generated by this procedure, the predicted changes to the UV/Vis spectra underestimate the observed changes for metal-free and nickel porphyrins. However, UV/Vis spectroscopy probes the relative energies of the porphyrin p-based MOs and here we are concerned with the spatial distributions and relative energies of the Fe 3d-based MOs.
70. Neese F. J. Chem. Phys. 2005; 122:034107.
71. Neese F. Inorg. Chim. Acta. 2002; 337:181–192.
72. Kutzelnigg, W.; Fleischer, U.; Schindler, M. The IGLO-Method: Ab Initio Calculation and Interpretation of NMR Chemical Shifts and Magnetic Susceptibilities. Vol. Vol. 23. Heidelberg, Germany: Springer-Verlag; 1990.
73. Neese F. J. Am. Chem. Soc. 2006; 128:10213–10222. [PubMed: 16881651]
74. Bergman DL, Laaksonen L, Laaksonen A. J. Mol. Graphics Modell. 1997; 15:301–306.
75. Laaksonen L. J. Mol. Graphics. 1992; 10:33–34.
76. Laaksonen, L. gOpenMol 2.32. Espoo, Finland: Center for Scientific Computing; 2002.
77. One of the four heme meso cross peaks was buried under the water band in the 1H-13C HMQC spectra of Q64V and A7F/Q64V 5-13C-ALA Ht cyt c552, but all four 13C resonances were identified in a 1-D 13C NMR spectrum collected without proton decoupling.
78. Bren, KL. Applications of Physical Methods to Inorganic and Bioinorganic Chemistry. Scott, RA.; Lukehart, CM., editors. Chichester, UK: John Wiley & Sons Ltd.; 2007. p. 357-384.
79. Walker FA. Inorg. Chem. 2003; 42:4526–4544. [PubMed: 12870942]
80. Santos H, Turner DL. Eur. J. Biochem. 1992; 206:721–728. [PubMed: 1318834]
81. Goff HM. J. Am. Chem. Soc. 1981; 103:3714–3722.
82. Johansson MP, Sundholm D, Gerfen G, Wikström M. J. Am. Chem. Soc. 2002; 124:11771–11780. [PubMed: 12296745]
83. La Mar, GN. NMR of Paramagnetic Molecules. La Mar, GN.; Horrocks, WD.; Holm, RH., editors. New York, NY: Academic Press; 1973. p. 85-126.
84. Kamiya K, Yamamoto S, Shiraishi K, Oshiyama A. J. Phys. Chem. B. 2009; 113:6866–6872. [PubMed: 19371055]
85. Michel LV, Ye T, Bowman SEJ, Levin BD, Hahn MA, Russell BS, Elliott SJ, Bren KL. Biochemistry. 2007; 46:11753–11760. [PubMed: 17900177]
86. Gouterman M. J. Chem. Phys. 1959; 30:1139–1161.
87. Marcus RA, Sutin N. Biochim. Biophys. Acta. 1985; 811:265–322.
88. Takayama SJ, Irie K, Tai HL, Kawahara T, Hirota S, Takabe T, Alcaraz LA, Donaire A, Yamamoto Y. J. Biol. Inorg. Chem. 2009; 14:821–828. [PubMed: 19294434]
89. Ma J-G, Zhang J, Franco R, Jia S-L, Moura I, Moura JJG, Kroneck PMH, Shelnutt JA. Biochemistry. 1998; 37:12431–12442. [PubMed: 9730815]

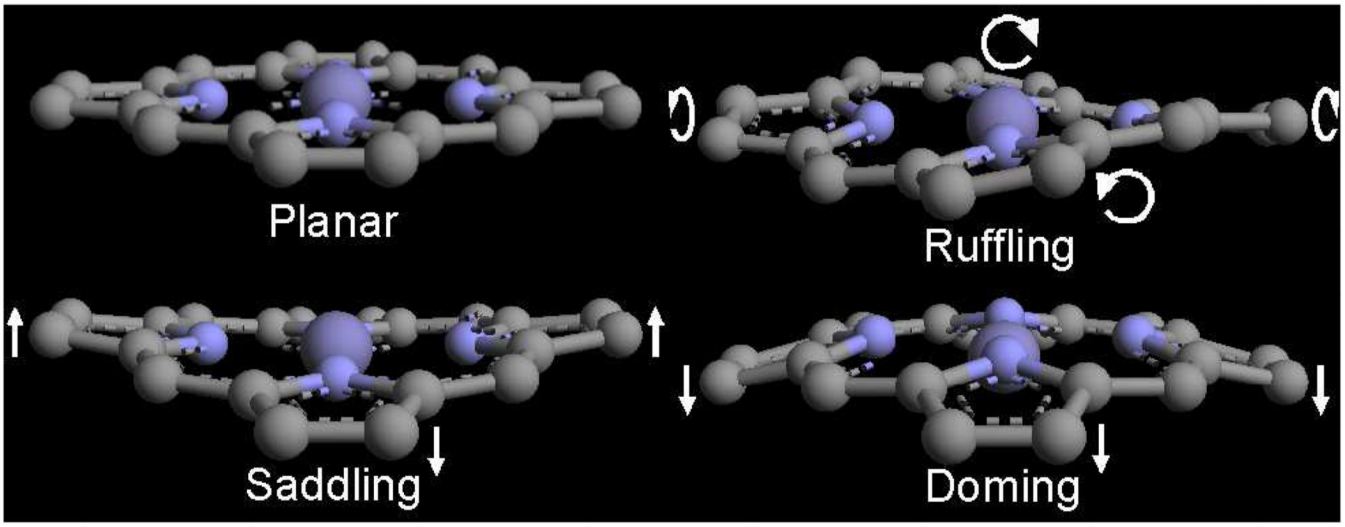

Figure 1.

The three most prevalent OOP distortions of the heme cofactor in biological systems are ruffling, saddling, and doming.1 The ruffling deformation is alternating clockwise and counterclockwise twisting of the pyrrole rings along the Fe–N axes. The saddling deformation is a bending of two pyrrole rings downward and two pyrrole rings upward with respect to the porphyrin plane, while doming is a concerted bending of all four pyrrole rings.

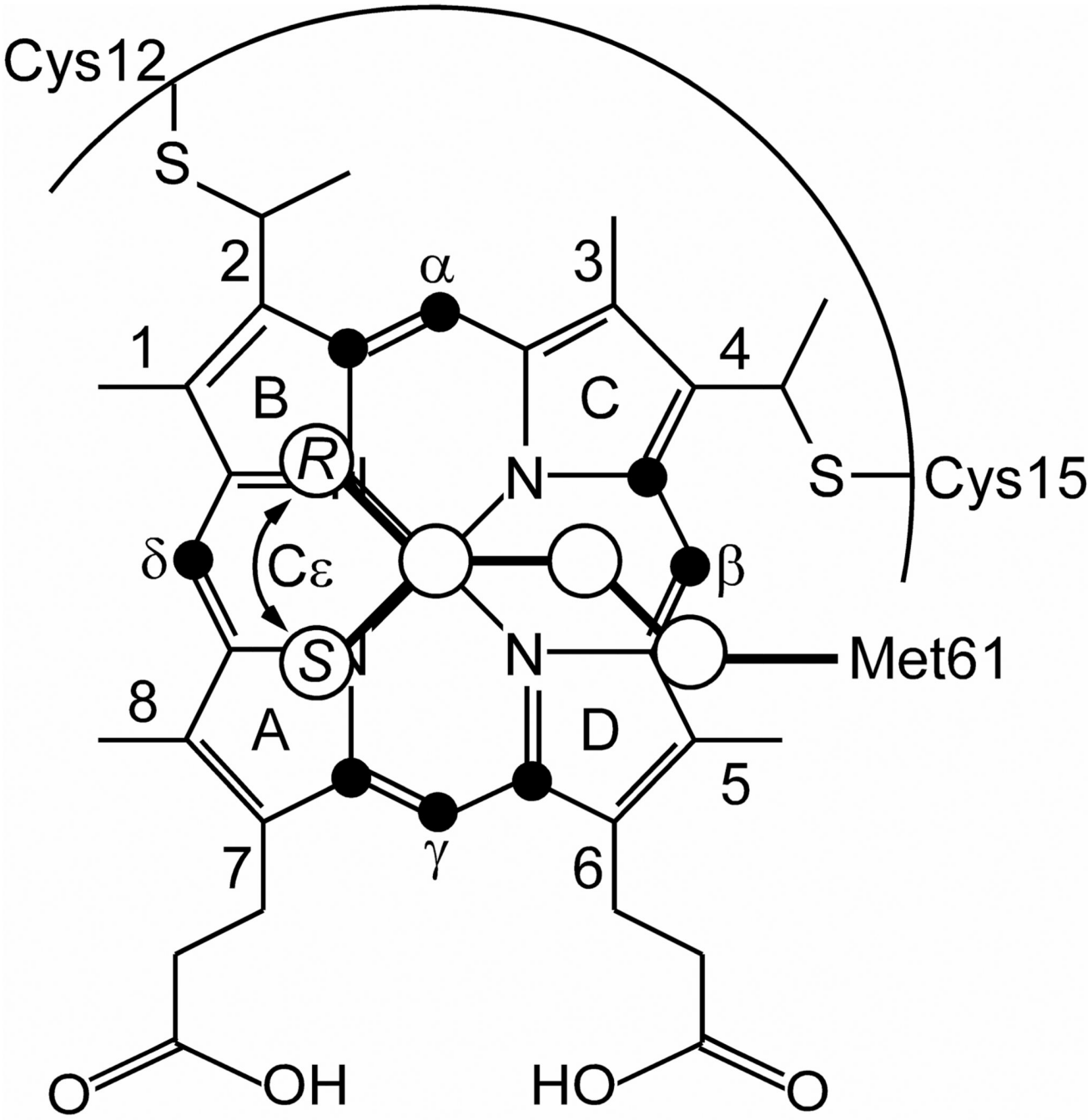

Figure 2.

The heme *c* cofactor contains a central Fe coordinated equatorially by the porphyrin macrocycle, which is covalently tethered to the polypeptide via two thioether bonds with a conserved CXXCH motif. The porphyrin ring consists of four pyrrole rings (labeled A, B, C, and D) linked by four meso carbons (labeled α, β, γ, and δ) with four methyl groups attached to the periphery (labeled 1, 3, 5, and 8). Typically, the Fe is axially coordinated by one His and one Met residue. The axial Met residue may adopt three different configurations: *R*, *S*, or fluxional, where the Met Cε rapidly samples both the *R* and *S* configurations. A change between the *R* and *S* configurations results in a different ligand orientation relative to the

heme plane. The heme meso carbons, as well as four additional α-pyrrole carbons identified by solid black circles are ^{13}C-enriched in 5-^{13}C-ALA *Ht* cyt c_{552}.47

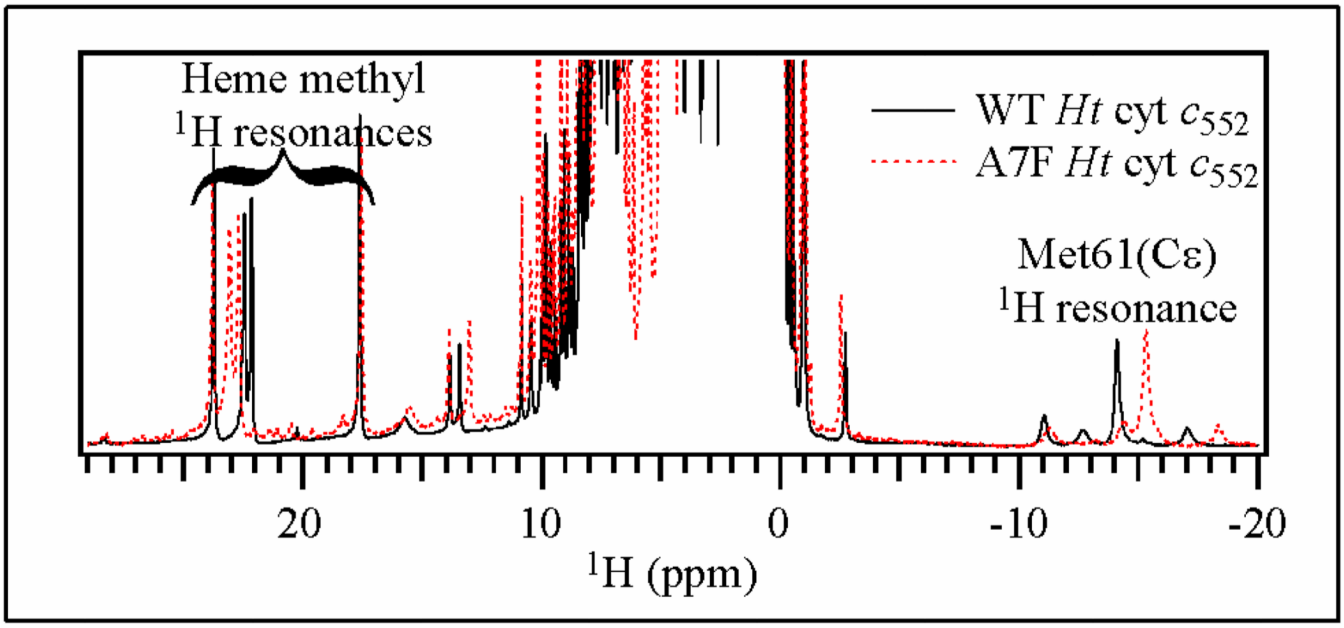

Figure 3.
^{1}H NMR spectra of 3.0 mM, oxidized WT and A7F *Ht* cyt c_{552} in 45 mM sodium phosphate buffer, pH = 7.0, at 51 °C. The four heme methyl ^{1}H resonances are shifted downfield in A7F *Ht* cyt c_{552} relative to WT, while the ^{1}H resonance of the axial Met(Cε) is shifted upfield.

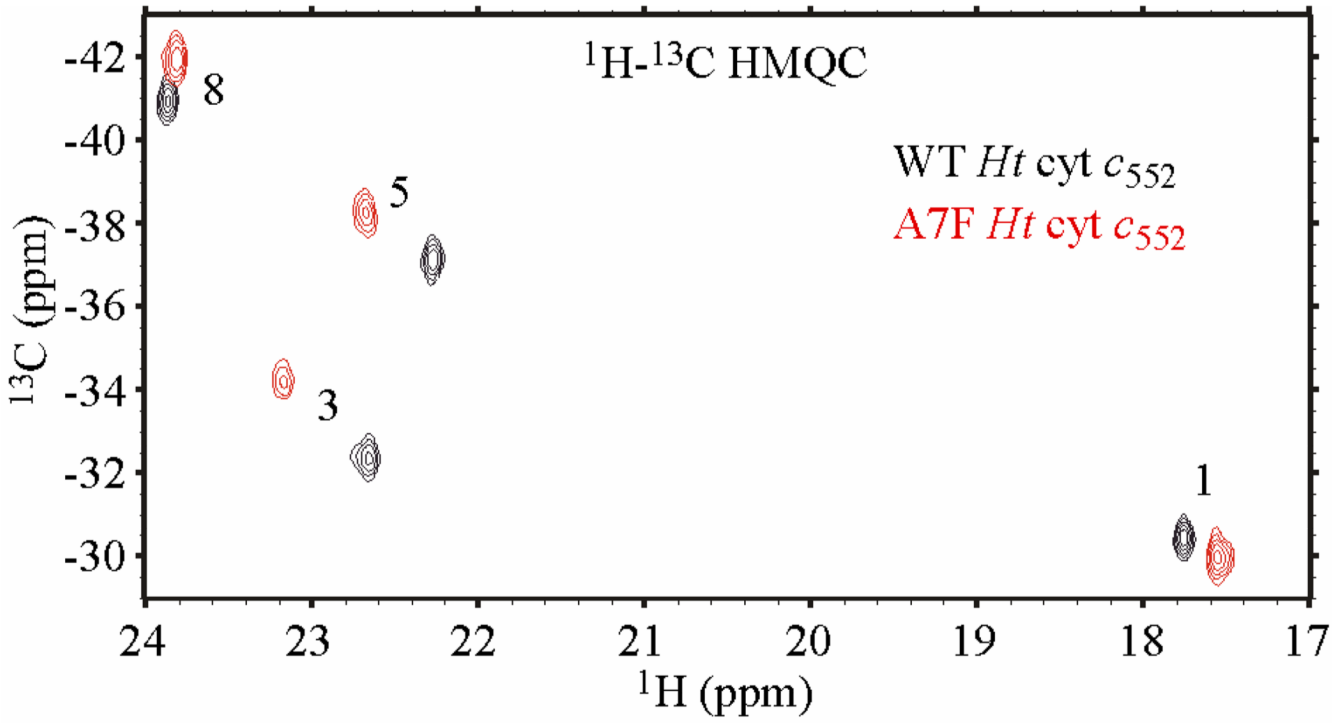

Figure 4.
The segment of the ^{1}H-^{13}C HMQC spectra of oxidized, natural isotopic abundance, WT and A7F *Ht* cyt c_{552} (3.0 mM) in 45 mM sodium phosphate buffer, pH = 7.0, at 51 °C that contains the four heme methyl ^{1}H-^{13}C cross peaks.

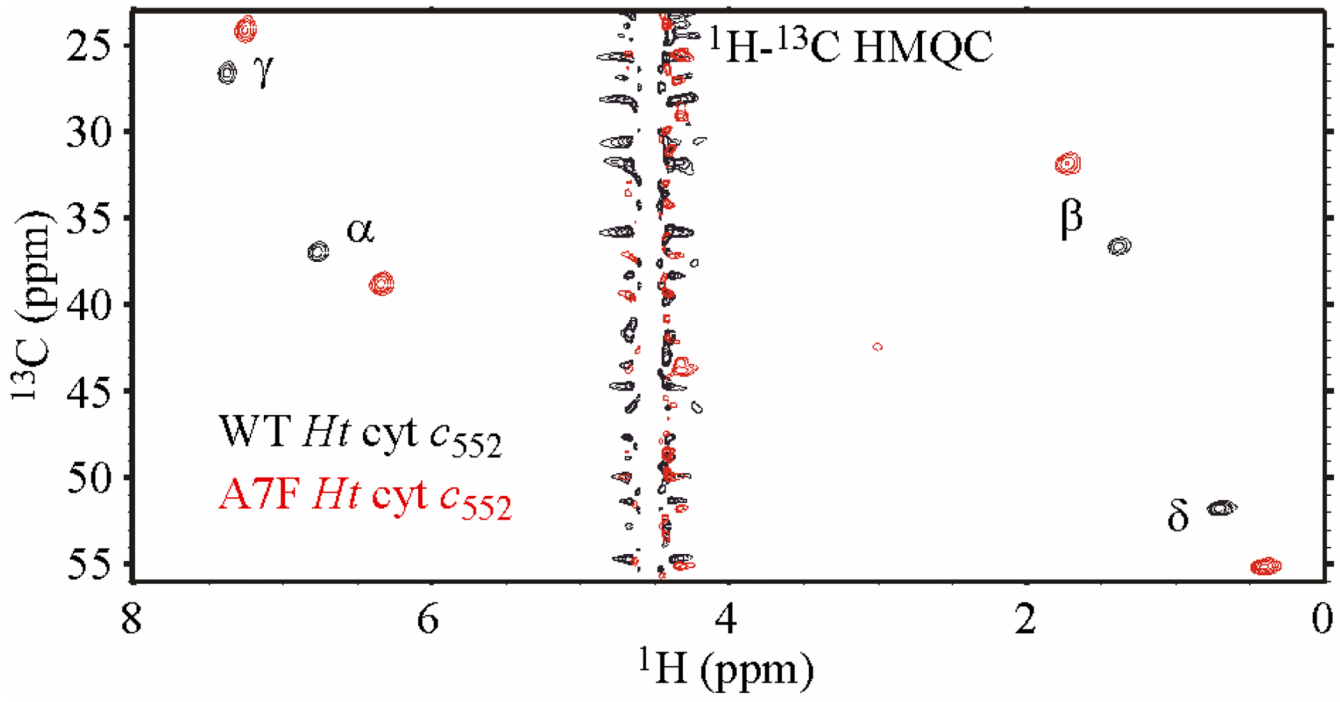

Figure 5.
^{1}H-^{13}C HMQC spectra of 1–2 mM, oxidized WT and A7F 5-^{13}C-ALA *Ht* cyt c_{552} in 45 mM sodium phosphate buffer, pH = 7.0, at 51 °C.

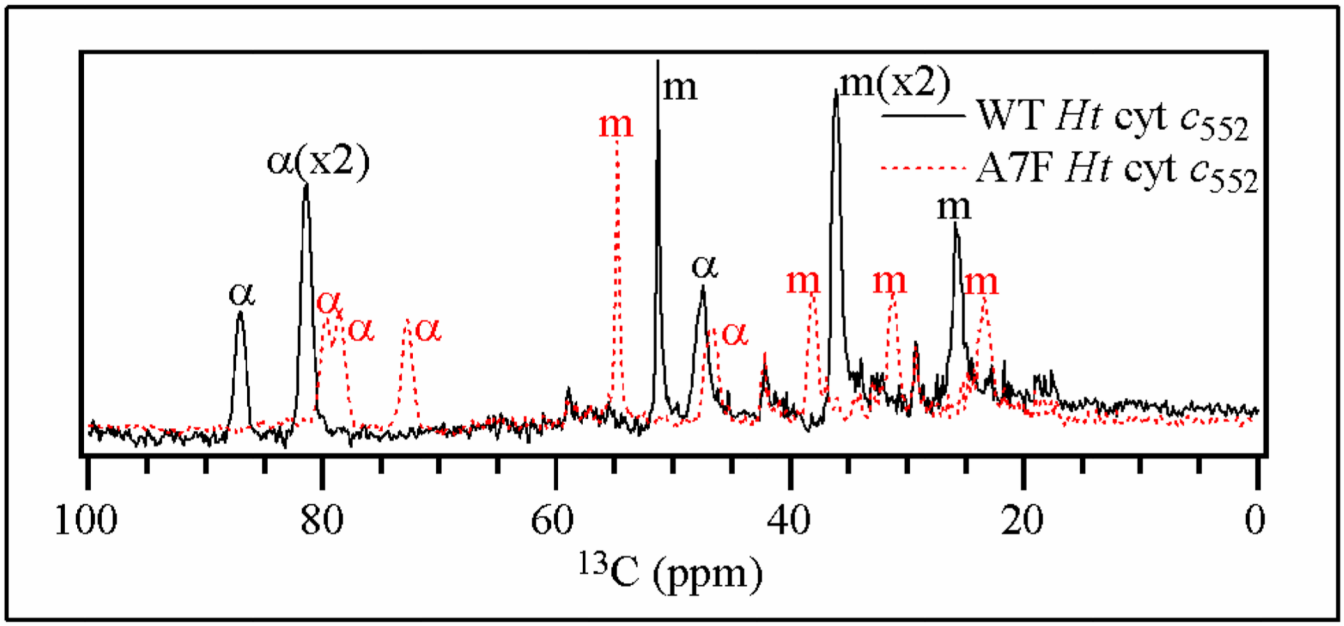

Figure 6.

^{13}C NMR spectra of 1–2 mM, oxidized WT and A7F 5-^{13}C-ALA *Ht* cyt c_{552} in 45 mM sodium phosphate buffer, pH = 7.0, at 51 °C, where the four heme meso (m) and four of the eight α-pyrrole carbons are ^{13}C-enriched (Figure 2).

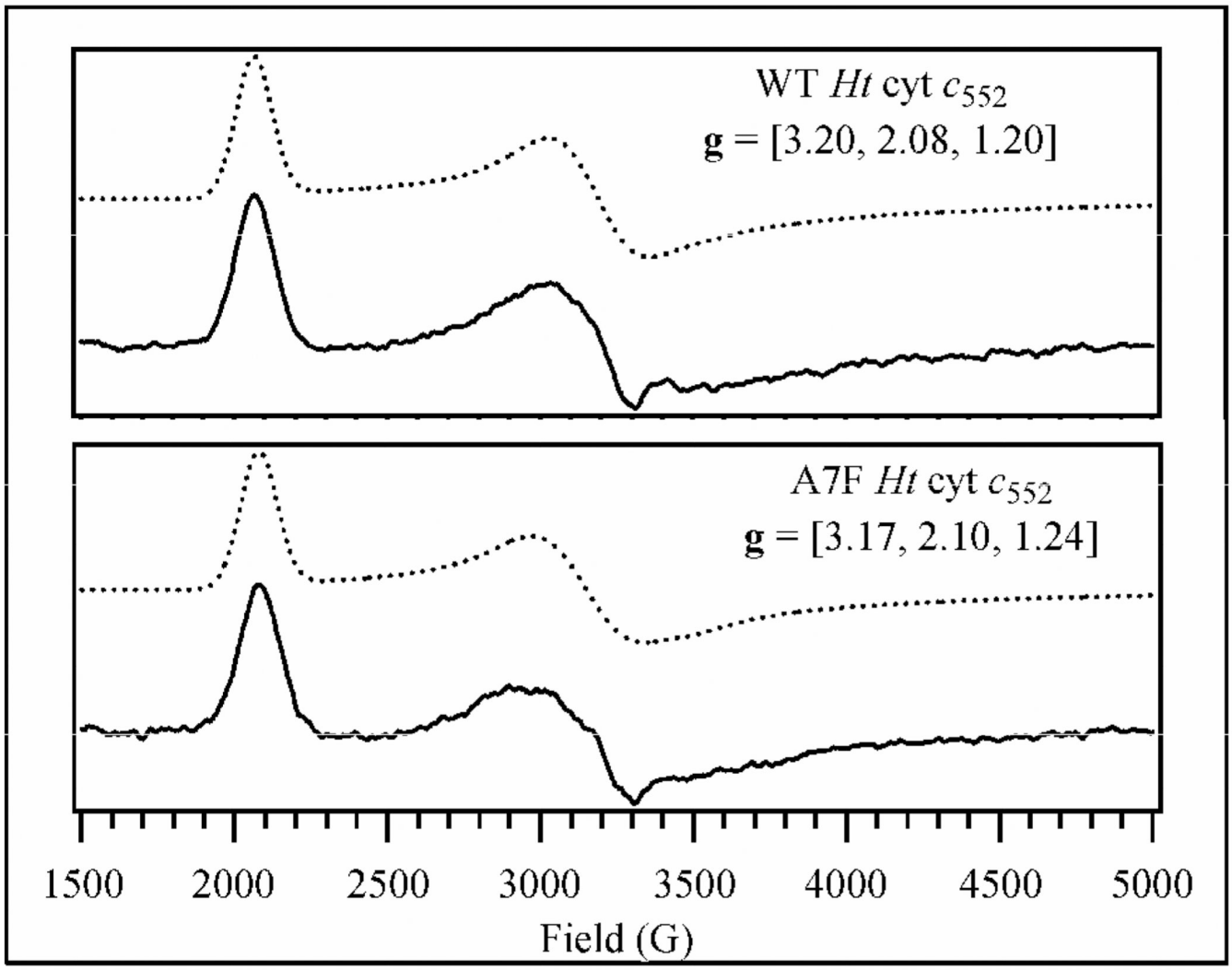

Figure 7.
X-Band (9.2 GHz) EPR spectra of WT and A7F *Ht* cyt c_{552} collected at 10 K with a microwave power of 200 μW, a modulation amplitude of 15 G, a modulation frequency of 100 kHz, and a time constant of 164 ms. Solid lines, experiment; Dotted lines, simulation using equation 2.

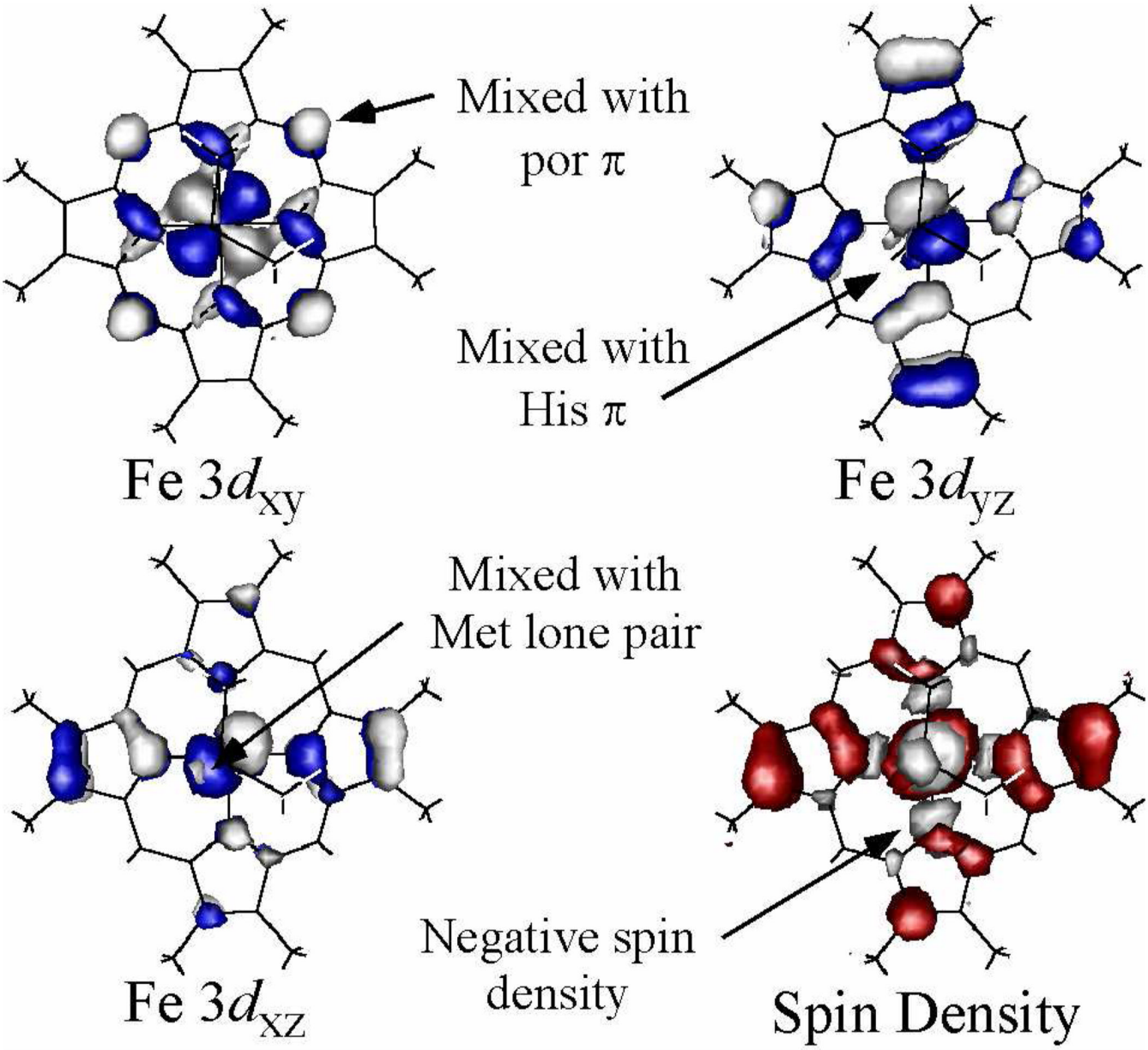

Figure 8.

PBE/TZVP occupied Fe 3*d*-based MOs and unpaired spin density of low-spin, Fe(III), His/Met-ligated heme (*R* Met). The electron density is delocalized on the ligands in all three Fe 3*d*-based MOs. The positive spin density (red) arises from single occupation of the Fe 3d_{xz}-based MO by a spin-up electron whereas the negative spin density (gray) is a consequence of electron exchange and correlation.

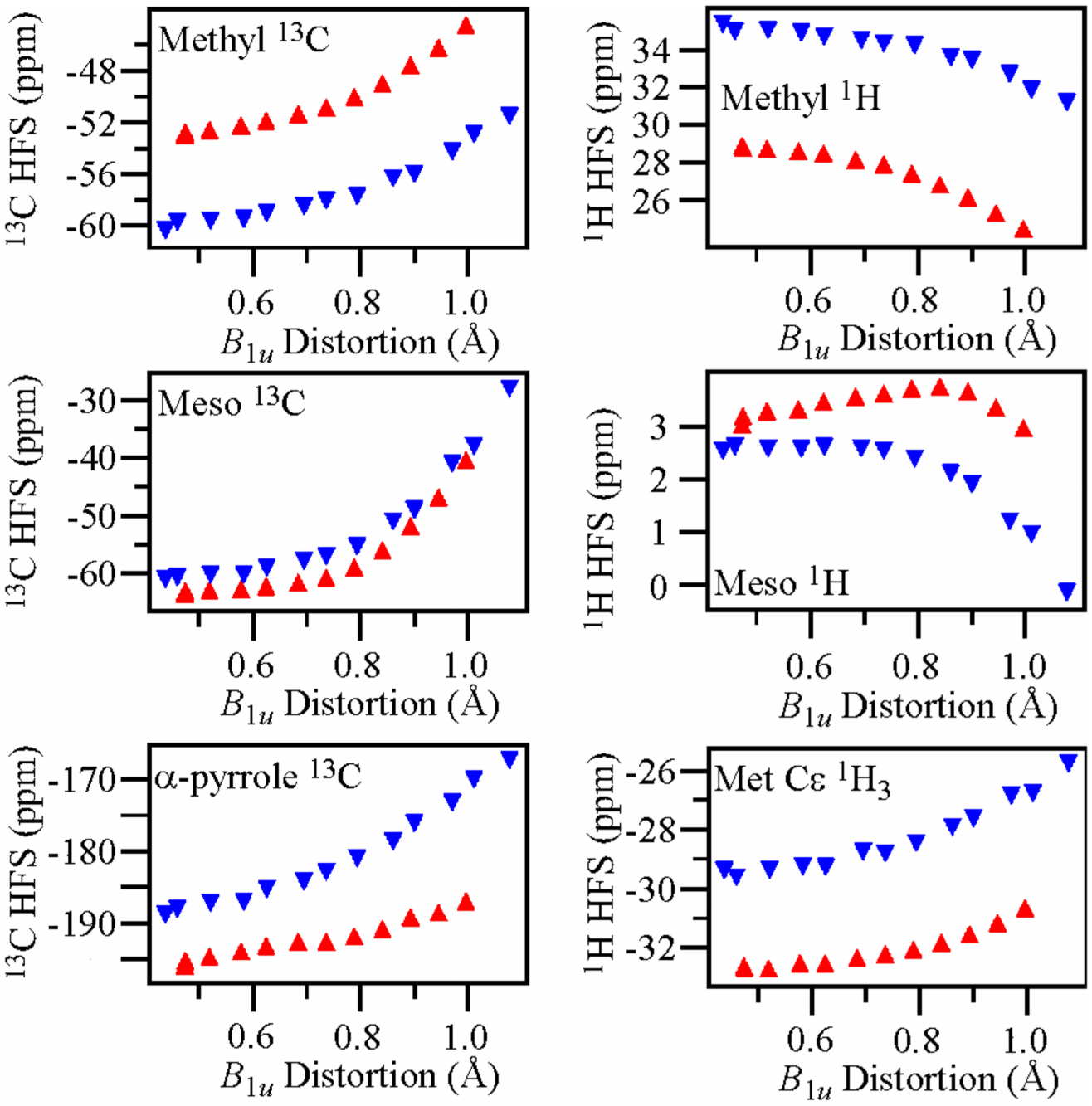

Figure 9.

PBE/IGLOIII ^{13}C and ^{1}H NMR HFSs of low-spin, His/Met-ligated heme at 25 °C calculated using equation 1 for *R* (upward red triangles) and *S* (downward blue triangles) configurations at the axial Met. The CP(PPP) basis set was used for the Fe(III) center. The magnitude of the B_{1u} distortion for each point along the ruffling deformation coordinate was determined using the Normal-Coordinate Structural Decomposition procedure of Shelnutt and co-workers.2

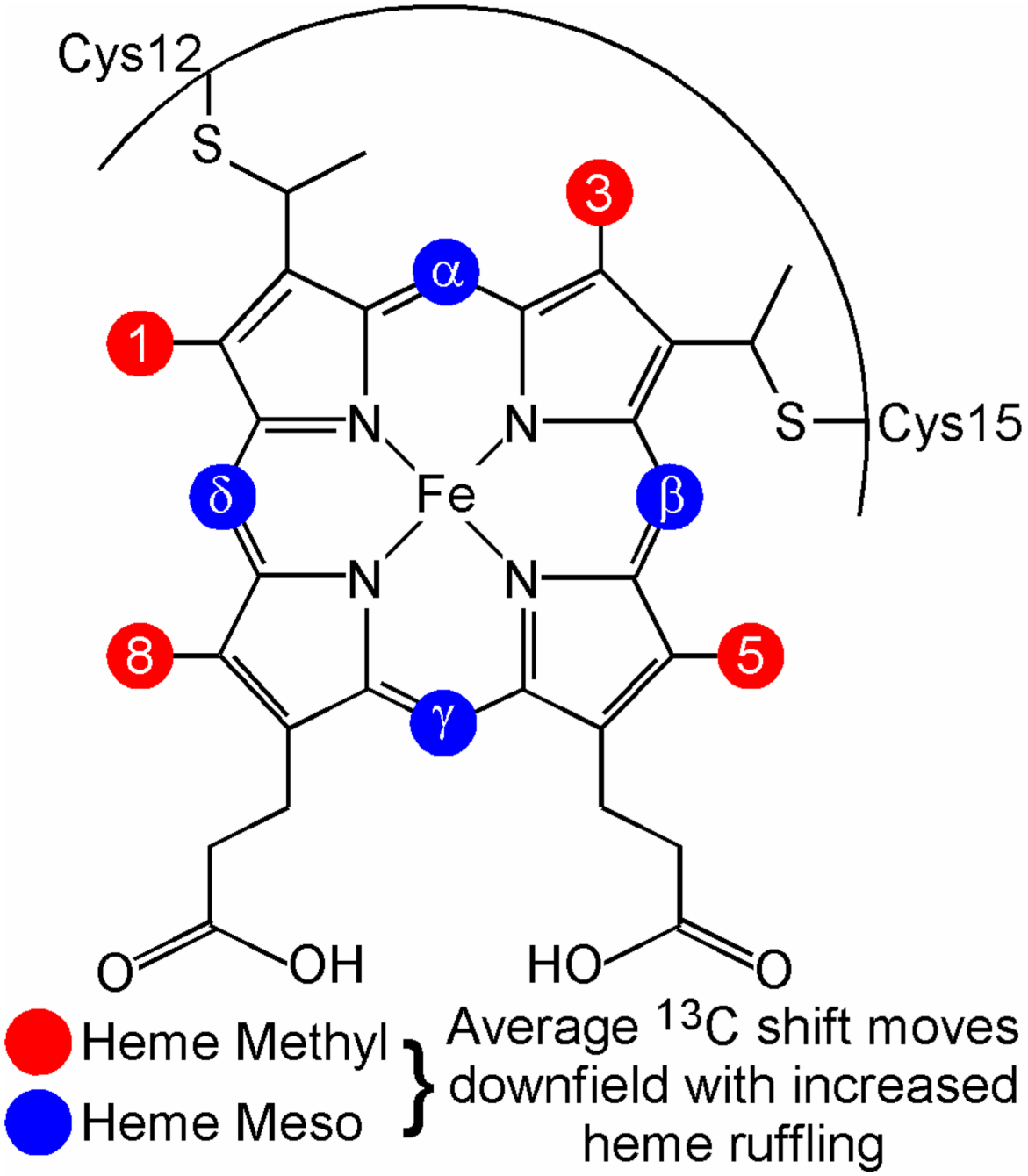

Scheme 1.

Table 1

Average heme methyl ^{1}H and ^{13}C shifts (ppm) for all six variants of *Ht* cyt c_{552} discussed in this work

^{1}H	**WT[a]**	**Q64N[b]**	**Q64V[b]**
WT	21.64	22.27	21.17
A7F	21.81	22.51	21.57
ΔA7F	0.17	0.24	0.40
^{13}C	WT[a]	Q64N[b]	Q64V[b]
WT	−35.2	−40.7	−39.8
A7F	−36.1	−41.3	−40.5
ΔA7F	−0.9	−0.7	−0.7

[a] Shifts measured at 51 °C.

[b] Shifts measured at 27 °C.

Table 2

Average heme meso ^{1}H and ^{13}C shifts (ppm) for *Ht* cyt c_{552}

^{1}H	**WT[a]**	**Q64N[b]**	**Q64V[c]**
WT	4.06	2.88	N.D.
A7F	3.93	2.70	N.D.
ΔA7F	−0.13	−0.18	N.D.
^{13}C	WT[a]	Q64N[b]	Q64V[b]
WT	38.0	32.7	31.3
A7F	37.4	32.5	31.0
ΔA7F	−0.5	−0.2	−0.3

[a] Shifts measured at 51 °C.

[b] Shifts measured at 27 °C.

[c] The heme α-meso ^{1}H resonance is obscured by the $^{1}H_2O$ peak at 27 °C.

Table 3

Met Cε^{1}H$_3$ shift and average ^{13}C shift (ppm) for the four ^{13}C-enriched α-pyrrole carbons of 5-^{13}C-ALA *Ht* cyt c_{552}

^{1}H	**WT**[a]	**Q64N**[b]	**Q64V**[b]
WT	−14.12	−14.92	−19.16
A7F	−15.33	−15.55	−20.21
ΔA7F	−1.21	−0.63	−1.05
^{13}C	WT[a]	Q64N[b]	Q64V[b]
WT	74.3	49.9	49.0
A7F	69.4	47.2	48.4
ΔA7F	−4.9	−2.8	−0.6

[a] Shifts measured at 51 °C.

[b] Shifts measured at 27 °C.

Table 4

LFT terms and HOMO description for WT and A7F *Ht* cyt c_{552}55

	WT	A7F
g_x	1.20 ± 0.04	1.24 ± 0.04
g_y	2.08 ± 0.01	2.10 ± 0.01
g_z	3.20 ± 0.01	3.17 ± 0.01
V/ξ	1.3 ± 0.1	1.3 ± 0.1
Δ/ξ	3.2 ± 0.2	3.3 ± 0.2
V/Δ	0.39 ± 0.07	0.41 ± 0.07
Fe d_{yz}	85.4 ± 0.7%	86.2 ± 0.7%
Fe d_{xz}	12.3 ± 0.7%	11.5 ± 0.6%
Fe d_{xy}	2.4 ± 0.3%	2.3 ± 0.3%